System analyses and motion control of a towed underwater vehicle

Master's Thesis

SYSTEM ANALYSES AND MOTION CONTROL OF A TOWED UNDERWATER VEHICLE

March 2015

Graduate School of Marine Science and Technology
Tokyo University of Marine Science and Technology
Master's Course of Marine System Engineering

ASUMA MINOWA

［修士］

修士学位論文内容要旨
Abstract

専　攻 Major	Marine System Engineering	氏　名 Name	Asuma Minowa
論文題目 Title	System analyses and motion control of a towed underwater vehicle		

This thesis presents system analyses and a motion control method for a towed underwater vehicle (TUV) which has movable wings at the center (main wing) and rear (tail wing) to actively control its attitude and depth. In recent years, some environmental problems such as global warming have become serious and, accordingly, importance of exploration of underwater environments have increased. A TUV is a kind of underwater vehicle which does not have a thruster inherently and is towed by the mothership to move. In the past, a lot of works on control problems of TUVs have been conducted, however there are few ones which address the system nonlinearity directly. Hence, our objective is to develop a motion control method for such a TUV taking account its nonlinearity.

First, the dynamical model in the lowest-order case is derived by using the Lagrange equations of motion and the principle of virtual work. To obtain the model, we employ two different approximate methods for the cable: the one is based on the lumped-mass method, and the other one regards the cable as a rigid bar.

Next, we locate an equilibrium point of the system such that attitudes of the vehicle and the main wing are horizontal. The linearization of the system around the point is obtained, and some basic characteristics of the system, i.e., stability, controllability and observability are analyzed. Based on these analyses, a linear state-feedback controller is initially designed to regulate the system to the equilibrium. Then, to develop output-feedback controllers, two types of nonlinear observers are constructed: one of which is based on the concept of high-gain observers, while the other one is consists of a linear Kalman filter gain and the original nonlinear model.

Finally, simulations of motion control to regulate the system to the equilibrium are performed to compare control performances of the output-feedback controllers and results from the different ways of approximation for the flexible cable. Those results show that for each model the high-gain observer approach reveals better performance than the other one. Therefore, we have confirmed that the proposed approach based on the high-gain observer is feasible and effective.

Contents

1 INTRODUCTION

1.1 Background

In general, there are various reasons for investigate underwater environments. Some of them have biological or ecological motives; behaviors of marine lives, biodiversities and the balance of ecosystems. Others are from the viewpoint of utilization of marine resources and space, for example fisheries management, seabed resources and submarine cable communication systems. Further, some environmental problems such as global warming or marine pollution have become serious.

Oceanographic research has a history of over 130 years and it has started with a voyage of the *Challenger* [1]. A significant amount of work has been devoted to investigate and monitor marine environments since then. In recent years, researchers have developed some approaches for offshore observations; Conductivity Temperature Depth (CTD) profiler with water samplers and remote sensing such as an application of satellites, for instance.

While an observation platform is determined by considering some points, especially characteristics of the targeted environment and spatial-temporal scales [2]. Kroger et al. [3] has summarized these situations and given overview of observational devices, which include buoys, ships, underwater vehicles and so on. Oceanographers practically utilize some of those devices to cover the deficiency of each method. For example, samplings by ships provide direct and stationary vertical profiles, and buoys and satellites are mainly employed in surface layer of the ocean for several months. Spatially continuous observations in the ocean are performed by submersible and horizontally movable devices such as an Argo float. Argo is a global array for temperature and salinity profiling floats, and the Argo project is one of the most famous and international approach for collecting the data of the mid or subsurface layer, providing real time data [4].

For more detailed exploration of the deep water layer or bottom of the ocean, unmanned underwater vehicles such as Autonomous Underwater Vehicles (AUVs) and Remotely Operated Vehicles (ROVs) are now very effective means of observing underwater environments. For example, the maturity and contributions of these vehicles have been reported [5]-[9]. Their aim is originally a seabed mapping but recently it has changed and expanded [9]. Because various kinds of instrumentation can be loaded in both vehicles, e.g., CTD sensors, Acoustic Doppler Current profilers (ADCPs) and cameras. Then spatial data and a synoptic view of the deep-sea are remarkably improved.

On the other hand, cost efficiency is another viewpoint of choosing observatories; design and improve of low-cost instruments for an oceanographic research are desirable [10]. In particular, AUVs and ROVs cost a lot to develop and include a problem in a power supply and navigation, which is crucial for operation [11]. So, developing alternative platforms or methods for a seabed survey are required.

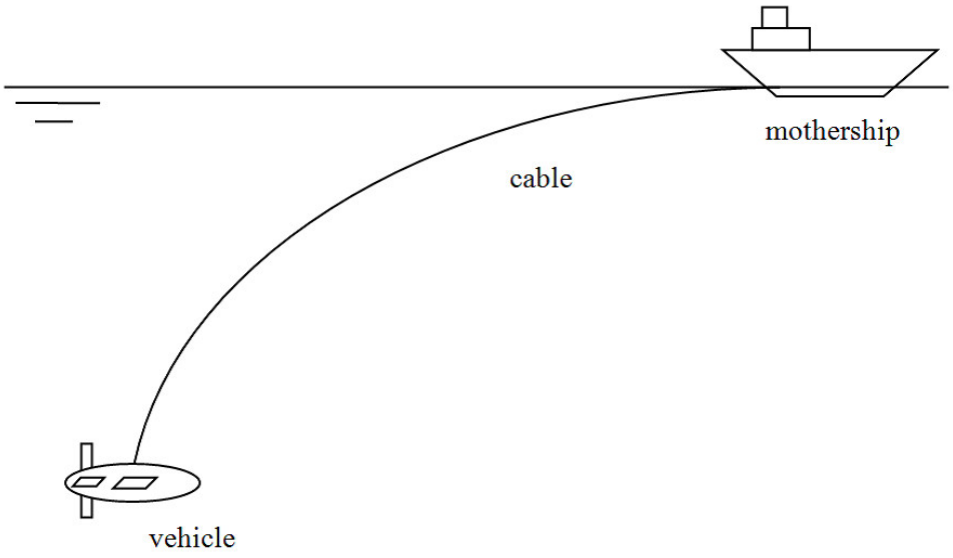

Figure 1: Schematic diagram of a TUV of single-part arrangement

Considering this situation, we focus on towed underwater vehicles (TUVs). A TUV does not have a thruster itself and needs to be towed by a mother ship to travel as shown in Fig. 1. They are low-cost devices compared with AUVs or ROVs and don't suffer from the challenge of a power supply and navigation. Nevertheless TUVs have a problem in the observation precision; this type of vehicle has been used without active control in most practical applications. Advanced sensors such as ADCPs or cameras for real time research are obviously influenced by the stability of the platforms, so a low-cost active controller is required to make its observations more accurate.

1.2 Related works

A lot of efforts, e.g., [12]-[28], have been devoted to control problems of TUVs. They can be classified broadly into two groups by arrangement of a towing system [28]. One of which is two-part towing arrangement that consists of a primary long cable with a gravitational depressor and a secondary cable with a vehicle. This arrangement can reduce influence of the dynamics from the towing cable to the vehicle, while is rather complicated to deploy and in need of higher cost for practical applications [22]-[26]. From these points of view, the other towing arrangement is more suitable for developing low-cost platforms. It is a single-part one, in which only a single long cable is connected to a vehicle directly.

Then one of obstacles for developing a control system for TUVs is dynamics of the flexible towing cable, which are highly complex and largely influential to the entire dynamics. A lot of researches for marine cable also have been done, e.g., [30]-[35]. However their approaches are based on the finite difference methods and among those methods the lumped-mass method may be the most conventional one [30]. In the lumped-mass approach the towing cable is modeled by some rigid segments, therefore the order of the

system relies on the number of the segment.

While the other serious issue to develop a control system for TUVs is highly-nonlinear dynamics affected by hydrodynamic forces; nevertheless there are few researches which consider nonlinearity of the system directly. One of the most interesting studies is presented by Teixeira et al. in 2006 [27] and 2010 [28]. They have designed a nonlinear adaptive controller and showed its good performance by simulations. But their target was the two-part towing arrangement and we can't apply this method promptly.

1.3 Purpose of the thesis

Previously, our group [20] has focused on TUVs of single-part arrangement as shown in Fig. 1, and analyzed a control system structure of TUVs. In this study the towing cable was modeled by the lumped-mass method and the Lagrange equation of motion was utilized. This paper has given an explicit formulation of state-space equations and a complete set of parameters for computation, and shown that the system has desirable properties in the sense of depth and attitude control.

In this thesis, based on [20], we present system analyses and a specific control design method for motion control of a TUV which is equipped with movable wings to control its depth and attitude. As the first step for the problem, the two types of dynamical models in the lowest-order case with relatively short towing cable are derived; one of which is based on the lumped-mass method, and the other one regards the cable as a rigid bar. We locate an equilibrium point and linearization around the point of each case is conducted. Some basic characteristics of the system are analyzed and, based on these analyses, a state-feedback controller for the approximately linearized system and observer-based output-feedback controllers are designed.

We employ and evaluate two types of nonlinear output-feedback controllers in this study; one of which is composed of a linear Kalman filter gain and the original nonlinear state-space model, while the other one is based on the concept of high-gain observers [29]. We demonstrate some control simulations to compare the performance of controllers and the effect of the difference of approximation of the flexible cable.

The remainder of this thesis will be organized as follows. In chapter 2, some assumptions are made and two cases of the dynamical model are formulated. The fundamental properties of the linearized system are verified in chapter 3. Then, in chapter 4, we propose a control design method and chapter 5 evaluates the designed controllers by simulations. In the last chapter, some concluding remarks are given.

2 DYNAMICAL MODEL

This chapter introduces some assumptions and a dynamical model for the study. Detailed parameters for computation and two types of coordinate systems are introduced. Then, we give explicit state-space representation of the dynamical system.

2.1 Problem setting

A TUV considered in this study is composed of a towing cable, torpedo-shaped main body and two movable wings to control its attitude and depth. To take the stage of the study and the order of the model into considertation, the total length of the cable is set as $L = 30$ (m). The length of the main body is nearly 1.4 m and the height is 0.41 m. We call the wings at the center of the vehicle as "main wing" and the rear one as "tail wing". Note that most of TUVs in practical use don't employ such maneuverable wings.

For simplicity, some assumptions are made in this thesis. At first, we restrict our interest to motions of the TUV on the vertical plane throughout this study, because such motions are the most important ones. Then, the following assumptions are made;

1. environmental water current will be ignored;
2. the dynamics of the mother ship and wing actuators will be ignored;
3. the mothership moves only in the horizontal direction with constant velocity v_0;
4. depth and attitude of the vehicle can be measured.

Parameters and their values adopted in this study are shown on Table 1, which are employed from the reference [17] and [20].

Table 1: Physical parameters

Symbol	Value	Unit
m_c	0.95	kg/m
a_c	$1.76715\rho \times 10^{-4}$	kg/m
B_c	0.69g	N/m
m_v	182.687	kg
B_v	0.162ρg	kg
a_{v11}	0.010ρ	kg
a_{v13}	0	kgm
a_{v22}	0.539ρ	kg
a_{v23}	0.032ρ	kgm
a_{v33}	0.039ρ	kgm^2
J_v	26.078	kgm^2
x_g	0.017	m
z_g	0.02	m
x_b	0.017	m
L	30	m
L_v	0.205	m
L_t	0.7	m
CD_{c1}	$-1.23075\rho \times 10^{-3}$	Ns^2/m^3
CD_{c2}	$3.975\rho \times 10^{-3}$	Ns^2/m^3
CL_{m1}	1.72595ρ	Ns^2/m^2
CL_{m2}	-0.141372	rad
CD_{m1}	0.60835ρ	Ns^2/m^2
CD_{m2}	0.00274506ρ	Ns^2/m^2
CL_{t1}	0.202770ρ	Ns^2/m^2
CD_{t1}	0.0335183ρ	Ns^2/m^2
CD_{t2}	$7.22347\rho \times 10^{-4}$	Ns^2/m^2
CL_{v1}	0.0766708ρ	Ns^2/m^2
CM	1.17268	m
g	9.8	m/s^2
ρ	1025	kg/m^3
v_0	4	m/s

2.2 Two types of dyanmical models

Generally, an underwater vehicle is modeled in a high-order system. But to take into account the stage of the study and from the viewpoint of control system design, a low-order system is desirable. In this thesis, we establish two types of dynamical models in the lowest-order case to design control systems; one of which is based on the lumped-mass method, and the other one regards the cable as a rigid bar. The lumped-mass method approximates the cable by one rigid segment with its mass concentrated at the end point, and all forces for the segment are assumed to be applied to the point of mass.

Fig. 2 shows the coordinate systems utilized for the lumped-mass case. $O_0X_0Z_0$ is the coordinate frame fixed at the towing point O_0 on the mothership. O_1 denotes the point of mass and $O_1X_1Z_1$ is the coordinate frame fixed on the cable and $O_2X_2Z_2$ is fixed at the center of the vehicle in like manner. Similarly, the coordinate systems for the rigid bar model are shown in Fig. 3. In this case, O_1 is located on the middle point of the cable, which denotes the center of gravity, and the axis Z_1 overlaps with the cable.

Then, generalized coordinates used for the dynamical model formulation are $q = [q_1, q_2]^T$, which are the attitudes of the cable and vehicle. The translational velocities O_1 and O_2 with respect to their own coordinates are represented by $v_1 = [v_{1x}, v_{1z}]^T$ and $v_2 = [v_{2x}, v_{2z}]^T$. Furthermore, the input angles of the main wing and the tail wing are denoted by u_1, u_2 respectively. Note that all the angles are defined to be positive in the counter-clockwise sense.

Based on the above problem setting and [20], we derive equations of motion. First, we calculate the total kinetic energy of each model. For the lumped-mass model, the inertia matrix for the cable segment is

$$M_1 = \begin{bmatrix} ma_c & 0 \\ 0 & ma_c \end{bmatrix}, \tag{1}$$

where $ma_c = L(m_c + a_c)$, and m_c and a_c denote the mass and the added mass of the cable per unit length. Second, M_2 denotes the inertia matrix of the vehicle and each element is represented as

$$\begin{aligned} M_2^{11} &= m_v + a_{v11} \\ M_2^{12} &= M_2^{21} = 0 \\ M_2^{13} &= M_2^{31} = m_v z_g + a_{v13} \\ M_2^{22} &= m_v + a_{v22} \\ M_2^{23} &= M_2^{32} = -m_v x_g + a_{v23} \\ M_2^{33} &= J_v + a_{v33} \end{aligned} \tag{2}$$

where m_v, a_{vij}, and J_v are the mass, the added inertias and the inertia moment of the vehicle respectively. Note that (x_g, z_g) denotes the coordinates of the center of gravity of the vehicle in $O_2X_2Z_2$. Then, the total kinetic energy for the lumped-mass model is represented by

$$\kappa = \frac{1}{2} v_1^T M_1 v_1 + \frac{1}{2} v_2^T M_2 v_2. \tag{3}$$

While we need to consider rotational motion of the cable for the rigid bar model; the kinetic energy of the cable is represented by

$$\kappa_1 = \frac{1}{2} v_1^T M_1 v_1 + \frac{1}{2} J \dot{q_1}^2, \tag{4}$$

where $J = \frac{1}{12} M_0 L^2$ denotes the inertia moment for the thin rigid bar and the total mass of the cable $M_0 = L m_c$. Then, the total kinetic energy for the rigid bar model is represented by

$$\kappa = \frac{1}{2} v_1^T M_1 v_1 + \frac{1}{2} J \dot{q_1}^2 + \frac{1}{2} v_2^T M_2 v_2. \tag{5}$$

Using resulting κ, we derive the Lagrange equations of motion for each case:

$$\frac{d}{dt}\left(\frac{\partial \kappa}{\partial \dot{q}}\right) - \frac{\partial \kappa}{\partial q} = E(q)\ddot{q} + F(q, \dot{q}), \tag{6}$$

where $E(q)$ is the inertia matrix, $F(q, \dot{q})$ is the Coriolis and centripetal force vector. The elements of the inertia matrix is represented as

$$E(q) = \begin{bmatrix} E_{11} & E_{12} \\ E_{21} & E_{22} \end{bmatrix}, \tag{7}$$

where

$$\begin{aligned}
E_{11} &= \frac{1}{2} L^2 \{(M_2^{11} + M_2^{22} + 2ma_c) + (M_2^{11} - M_2^{22}) c(2q_1 - 2q_2)\}, && (8)\\
E_{12} &= E_{21} && (9)\\
&= L\{(M_2^{13} + L_v M_2^{11}) c(q_1 - q_2) - M_2^{23} s(q_1 - q_2)\}, && (10)\\
E_{22} &= M_2^{33} + L_v(2M_2^{13} + L_v M_2^{11}) && (11)
\end{aligned}$$

for the lumped-mass model. $s(\cdot)$ and $c(\cdot)$ are the abbreviations of $\sin(\cdot)$ and $\cos(\cdot)$ respectively and $(0, -L_v)$ denotes the towing point on the vehicle in $O_2 X_2 Z_2$. We also obatin

$$\begin{aligned}
E_{11} &= L^2\{\frac{1}{4} m a_c + M_2^{11} c^2(q_1 - q_2) + M_2^{22} s^2(q_1 - q_2)\} + J, && (12)\\
E_{12} &= E_{21} \\
&= L\{(M_2^{13} + L_v M_2^{11}) c(q_1 - q_2) - M_2^{23} s(q_1 - q_2)\}, && (13)\\
E_{22} &= M_2^{33} + L_v(2M_2^{13} + L_v M_2^{11}) && (14)
\end{aligned}$$

for the rigid bar model. The elements of $F(q, \dot{q})$ for the lumped-mass model are represented

as

$$
\begin{aligned}
F_1 \;=& -\frac{1}{2}L^2(M_2^{11}-M_2^{22})s(2q_1-2q_2)\dot{q_1}^2 \\
&+ L^2(M_2^{11}-M_2^{22})s(2q_1-2q_2)\dot{q_1}\dot{q_2} \\
&+ L\{M_2^{23}c(q_1-q_2)+(M_2^{13}+L_vM_2^{11})s(q_1-q_2)\}\dot{q_2}^2 \\
&+ L(M_2^{11}-M_2^{22})s(q_1-2q_2)v_0\dot{q_2} \\
&+ \frac{1}{2}L\{(M_2^{11}-M_2^{22})c(q_1-2q_2)+(M_2^{11}+M_2^{22}+2ma_c)c(q_1)\}\dot{v_0}, \qquad (15) \\
F_2 \;=& -L\{\frac{1}{2}L(M_2^{11}-M_2^{22})s(2q_1-2q_2) \\
&+ M_2^{23}c(q_1-q_2)+(M_2^{13}+L_vM_2^{11})s(q_1-q_2)\}\dot{q_1}^2 \\
&- L(M_2^{11}-M_2^{22})s(q_1-2q_2)v_0\dot{q_1} \\
&+ \frac{1}{2}(M_2^{11}-M_2^{22})s(2q_2)v_0^2 \\
&+ \{M_2^{23}s(q_2)+(M_2^{13}+L_vM_2^{11})c(q_2)\}\dot{v_0}, \qquad (16)
\end{aligned}
$$

Similarly,

$$
\begin{aligned}
F_1 \;=& -\frac{1}{2}L^2(M_2^{11}-M_2^{22})s(2q_1-2q_2)\dot{q_1}^2 \\
&+ L^2(M_2^{11}-M_2^{22})s(2q_1-2q_2)\dot{q_1}\dot{q_2} \\
&+ L\{M_2^{23}c(q_1-q_2)+(M_2^{13}+L_vM_2^{11})s(q_1-q_2)\}\dot{q_2}^2 \\
&+ L(M_2^{11}-M_2^{22})s(q_1-2q_2)v_0\dot{q_2} \\
&+ \frac{1}{2}L\{(M_2^{11}+M_2^{22}+ma_c)c(q_1)+(M_2^{11}-M_2^{22})c(q_1-2q_2)\}\dot{v_0}, \qquad (17) \\
F_2 \;=& -L\{L(M_2^{11}-M_2^{22})s(q_1-q_2)c(q_1-q_2) \\
&+ M_2^{23}c(q_1-q_2)+(M_2^{13}+L_vM_2^{11})s(q_1-q_2)\}\dot{q_1}^2 \\
&- L(M_2^{11}-M_2^{22})s(q_1-2q_2)v_0\dot{q_1} \\
&+ \frac{1}{2}(M_2^{11}-M_2^{22})s(2q_2)v_0^2 \\
&+ \{M_2^{23}s(q_2)+(M_2^{13}+L_vM_2^{11})c(q_2)\}\dot{v_0} \qquad (18)
\end{aligned}
$$

for the rigid bar model.

Next, by applying the principle of virtual work, generalized forces that consist of buoyancy, gravity and hydrodynamic forces are given. τ_{bg} associated with buoyancy and gravity can be derived as

$$
\begin{aligned}
\tau_{bg1} &= L\{L(B_c-m_cg)+B_v-m_vg\}s(q_1), \qquad (19) \\
\tau_{bg2} &= \{B_vL_v-m_vg(L_v+z_g)\}s(q_2)+(B_vx_b-m_vgx_g)c(q_2) \qquad (20)
\end{aligned}
$$

for the the lumped-mass model, where B_c, g and B_v are the buoyancy of the cable per unit length, the gravitational acceleration and the buoyancy of the vehicle respectively.

$(x_b, 0)$ denotes the centor of buoyancy of the vehicle in $O_2X_2Z_2$. For the rigid bar model, we obatin

$$\tau_{bg1} = \frac{1}{2}L^2(B_c - m_c g)s(q_1) + L(B_v - m_v g)s(q_1), \tag{21}$$

$$\tau_{bg2} = \{B_v L_v - m_v g(L_v + z_g)\}s(q_2) + (B_v x_b - m_v g x_g)c(q_2). \tag{22}$$

Further, the hydrodynamic force vector τ_h of the lumped-mass model is represented as

$$\begin{aligned}\tau_{h1} =& -Lh_{c1}c(\alpha_1) \\ &+ L\{-h_{mD}c(\alpha_2 + q_1 - q_2) - h_{tD}c(\alpha_t + q_1 - q_2) \\ &+ (h_{vL} + h_{mL})s(\alpha_2 + q_1 - q_2) + h_{tL}s(\alpha_t + q_1 - q_2)\},\end{aligned} \tag{23}$$

$$\begin{aligned}\tau_{h2} =& L_v(h_{mL} + h_{vL})s(\alpha_2) - L_v h_{mD}c(\alpha_2) + h_{vL}CM \\ &+ (-L_t h_{tD} + L_v h_{tL})s(\alpha_t) - (L_v h_{tD} + L_t h_{tL})c(\alpha_t),\end{aligned} \tag{24}$$

where the suffix t denotes the tail wing, $(-L_t, 0)$ in $O_2X_2Z_2$ is the center of hydrodynamic force on tail wing and CM is a constant parameter related with hydrodynamic moment. $\alpha_i (i = 1, 2, t)$ denotes the angle of attack and is given by

$$\alpha_i = \tan^{-1}\left(\frac{v_{iz}}{v_{ix}}\right) \ (v_{ix} \neq 0). \tag{25}$$

The angle of attack for the tail wing α_t is given by the velocity vector $v_t = [v_{tx}, v_{tz}]^T$ at $(-L_t, 0)$ in $O_2X_2Z_2$. Besides, each of the hydrodynamic force h_χ is defined as in the following.

$$h_{c1} = L(CD_{c1}\alpha_1^2 + CD_{c2})\|v_1\|^2 \tag{26}$$

$$h_{mL} = CL_{m1}(\alpha_2 + u_1 + CL_{m2})\|v_2\|^2 \tag{27}$$

$$h_{mD} = \{CD_{m1}(\alpha_2 + u_1 + CL_{m2})^2 + CD_{m2}\}\|v_2\|^2 \tag{28}$$

$$h_{tL} = CL_{t1}(\alpha_t + u_2)\|v_t\|^2 \tag{29}$$

$$h_{tD} = \{CD_{t1}(\alpha_t + u_2)^2 + CD_{t2}\}\|v_t\|^2 \tag{30}$$

$$h_{vL} = CL_{v1}\alpha_2\|v_2\|^2 \tag{31}$$

where h_{c1} denotes the drag on the cable segment, the suffixes L and D denote the drag and the lift and the suffixes m and v represent the main wing and the vehicle, respectively. The constant parameters CD_χ and CL_χ are the drag and the lift coefficients and $||\cdot||$ represents the Euclidean norm. Again, u_1 is for the input angle of the main wing and u_2 for the tail wing. Finally,

$$\begin{aligned}\tau_{h1} =& -\frac{1}{2}Lh_{c1}c(\alpha_1) \\ &+ L\{-h_{mD}c(\alpha_2 + q_1 - q_2) - h_{tD}c(\alpha_t + q_1 - q_2) \\ &+ (h_{vL} + h_{mL})s(\alpha_2 + q_1 - q_2) + h_{tL}s(\alpha_t + q_1 - q_2)\},\end{aligned} \tag{32}$$

$$\begin{aligned}\tau_{h2} =& L_v(h_{mL} + h_{vL})s(\alpha_2) - L_v h_{mD}c(\alpha_2) + h_{vL}CM \\ &+ (-L_t h_{tD} + L_v h_{tL})s(\alpha_t) - (L_v h_{tD} + L_t h_{tL})c(\alpha_t)\end{aligned} \tag{33}$$

for the rigid bar model. It is natural that (20) and (22) are the same and so (24) and (33) respectively.

2.3 Derivation of state-space equatioins

Let the state vector $x = [x_1^T, x_2^T]^T = [x_{11}, x_{12}, x_{21}, x_{22}]^T = [q^T, \dot{q}^T]^T \in$ the state-space manifold $\mathcal{X} \subset \mathbf{R}^4$, the input vector $u = [u_1, u_2]^T \in \mathbf{R}^2$ and the output vector $y = [y_1, y_2]^T \in$ the output-space manifold $\mathcal{Y} \subset \mathbf{R}^2$. Then, the dynamical model is formulated as

$$E(x_1)\ddot{x} + F(x, \dot{x}) = \tau_{bg}(x_1) + \tau_h(x, u), \tag{34}$$

and is transformed into the following state-space representation

$$\begin{array}{rcl} \dot{x} & = & f(x, u) \\ y & = & h(x_1) \end{array} \tag{35}$$

where f and h are defined as

$$f(x, u) = \left[\begin{array}{c} x_2 \\ E(x_1)^{-1}\{-F(x) + \tau_{bg}(x_1) + \tau_h(x, u)\} \end{array} \right], \tag{36}$$

$$h(x_1) = \left[\begin{array}{c} L\cos\,(x_{11}) + L_v\cos\,(x_{12}) \\ x_{12} \end{array} \right]. \tag{37}$$

Note that the output y_1 is the depth of the center of the vehicle and y_2 is the attitude of the vehicle.

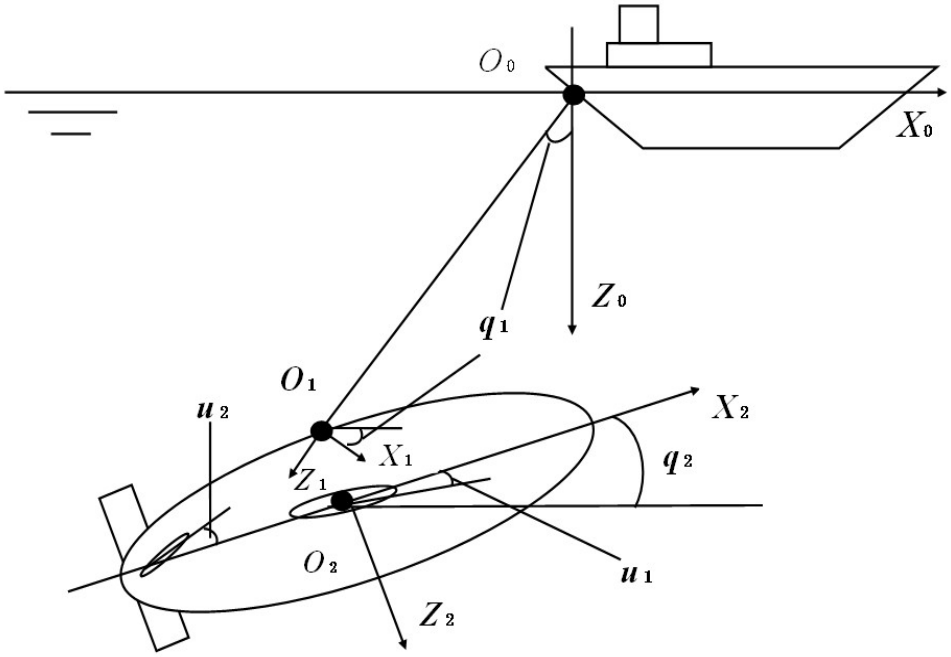

Figure 2: Coordinate systems for the lumped-mass model

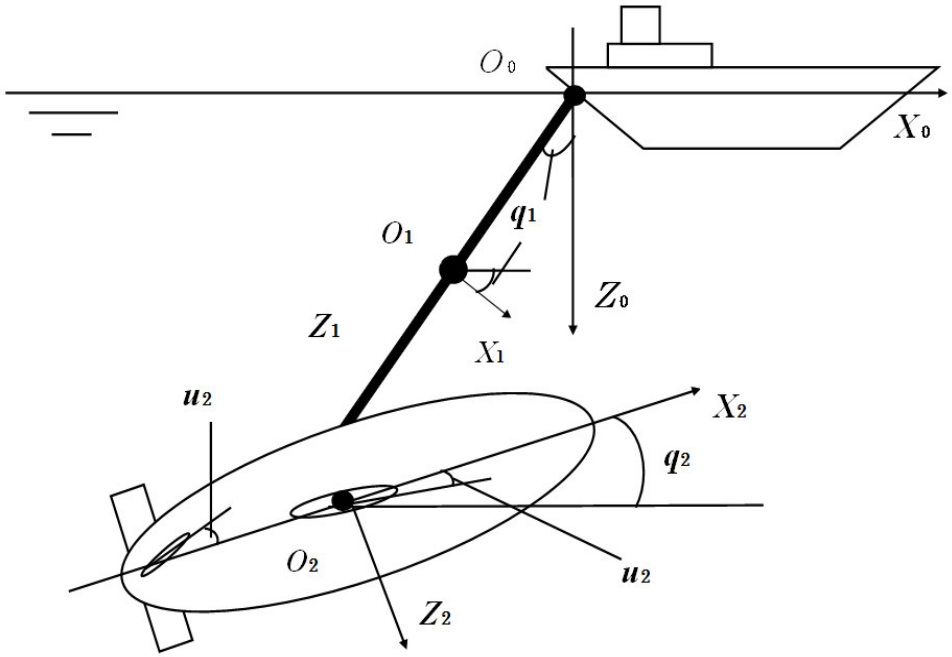

Figure 3: Coordinate systems for the rigid bar model

3 SYSTEM STRUCTURE ANALYSES

In this chapter, analyses of the control system structure are presented. We obtain an equilibrium point of each model and an approximate linearized system around the point. Then, some basic characteristics of the system such as stability, controllability and observability are analyzed.

3.1 Equilibrium point and linearization

First, an equilibrium point $x^* = [x_1^{*T}, x_2^{*T}]^T = [x_{11}^*, x_{12}^*, x_{21}^*, x_{22}^*]^T$ and $u^* = [u_1^*, u_2^*]^T$ of each system (35) satisfying $f(x^*, u^*) = 0$ is calculated. In this study, the attitude of the vehicle x_{12}^* and the angle of input for main wing u_1^* are assumed to be 0 (deg). Employing MATLAB function "fminsearch", we have obtained $x^* = [-25.8117, 0, 0, 0]^T$ and $u^* = [0, -1.3636]^T$ for the lumped-mass model and $x^* = [-15.7993, 0, 0, 0]^T$ and $u^* = [0, -1.3640]^T$ for the rigid bar model. Note that x_{11}^* of the lumped-mass model is smaller than that of the rigid bar model, while u_2^*'s are almost the same value.

Then, the approximate linearized system around (x^*, u^*) are derived as

$$\begin{aligned} \dot{w} &= Aw + Bv \\ p &= Cw, \end{aligned} \tag{38}$$

where $w = x - x^*$ and $v = u - u^*$. Each coefficient matrix is computed with

$$\begin{aligned} A &= \frac{\partial f}{\partial x}(x^*, u^*), \\ B &= \frac{\partial f}{\partial u}(x^*, u^*), \\ C &= \frac{\partial h}{\partial x}(x^*). \end{aligned} \tag{39}$$

Calculating by MATHEMATICA, we have obtained the coefficient matrices for the lumped-mass model

$$A = \begin{bmatrix} 0 & 0 & 1 & 0 \\ 0 & 0 & 0 & 1 \\ -0.6025 & -1.9483 & -8.4312 & -0.0860 \\ 12.9060 & 144.9450 & 521.2560 & -3.8120 \end{bmatrix}, \tag{40}$$

$$B = \begin{bmatrix} 0 & 0 \\ 0 & 0 \\ -1.1615 & 0.0266 \\ 32.8450 & -32.5671 \end{bmatrix}, \tag{41}$$

$$C = \begin{bmatrix} 13.0617 & 0 & 0 & 0 \\ 0 & 1 & 0 & 0 \end{bmatrix}, \tag{42}$$

while for the rigid bar model

$$A = \begin{bmatrix} 0 & 0 & 1 & 0 \\ 0 & 0 & 0 & 1 \\ -0.7318 & -1.8000 & -4.1314 & -0.0618 \\ 15.0193 & 140.1570 & 298.0650 & -4.3876 \end{bmatrix}, \tag{43}$$

$$B = \begin{bmatrix} 0 & 0 \\ 0 & 0 \\ -0.8552 & 0.1125 \\ 25.5190 & -34.3049 \end{bmatrix}, \tag{44}$$

$$C = \begin{bmatrix} 8.1681 & 0 & 0 & 0 \\ 0 & 1 & 0 & 0 \end{bmatrix}. \tag{45}$$

3.2 Analyses on control system structure

Based on the linearized system, let us consider the control system structure. First, to assess the stability of the equilibrium, the eigenvalues of matrix A are calculated. Employing MATLAB function "eig", we obtain $\{\lambda_1, \lambda_2, \lambda_3, \lambda_4\} = \{-15.7216, -1.9581, -0.3492, 5.7857\}$ for the lumped-mass model and $\{\lambda_1, \lambda_2, \lambda_3, \lambda_4\} = \{-15.1605, -0.2062+0.8147i, -0.2062-0.8147i, 7.0540\}$ for the rigid bar model. These results indicate that λ_4 of each system is an unstable mode.

Next, we construct the following matrices

$$W_c = \left[B, AB, A^2B, A^3B\right] \tag{46}$$

and

$$W_o = \left[C^T, (CA)^T, (CA^2)^T, (CA^3)^T\right]^T \tag{47}$$

to verify the controllability and observability. Computing the ranks of those matrices by MATLAB function "rank", we obtain the result that $\mathrm{rank}(W_c) = 4$ and $\mathrm{rank}(W_o) = 4$ for the lumped-mass model, and $\mathrm{rank}(W_c) = 4$ and $\mathrm{rank}(W_o) = 4$ for the rigid bar model; which implies each system is controllable and observable. Therefore, at least around the equilibrium point, we can design a stabilizing control system based on state-feedback controllers and observers.

In addition to this, Fig. 4 for the lumped-mass model and Fig. 5 for the rigid bar model show the frequency response of each control system. The upper figure corresponds to output 1 (depth of the vehicle) and the lower one for output 2 (attitude of the vehicle). The solid lines are associated with input 1 (main wing) and the dashed lines with input 2 (tail wing). As seen from these diagrams, input 1 of each case mainly affects the depth of the vehicle, while the attitude of the vehicle is mainly influenced by input 2, particularly over low frequencies. Hence we are convinced that the wing configuration is suitable for the control purpose of this study.

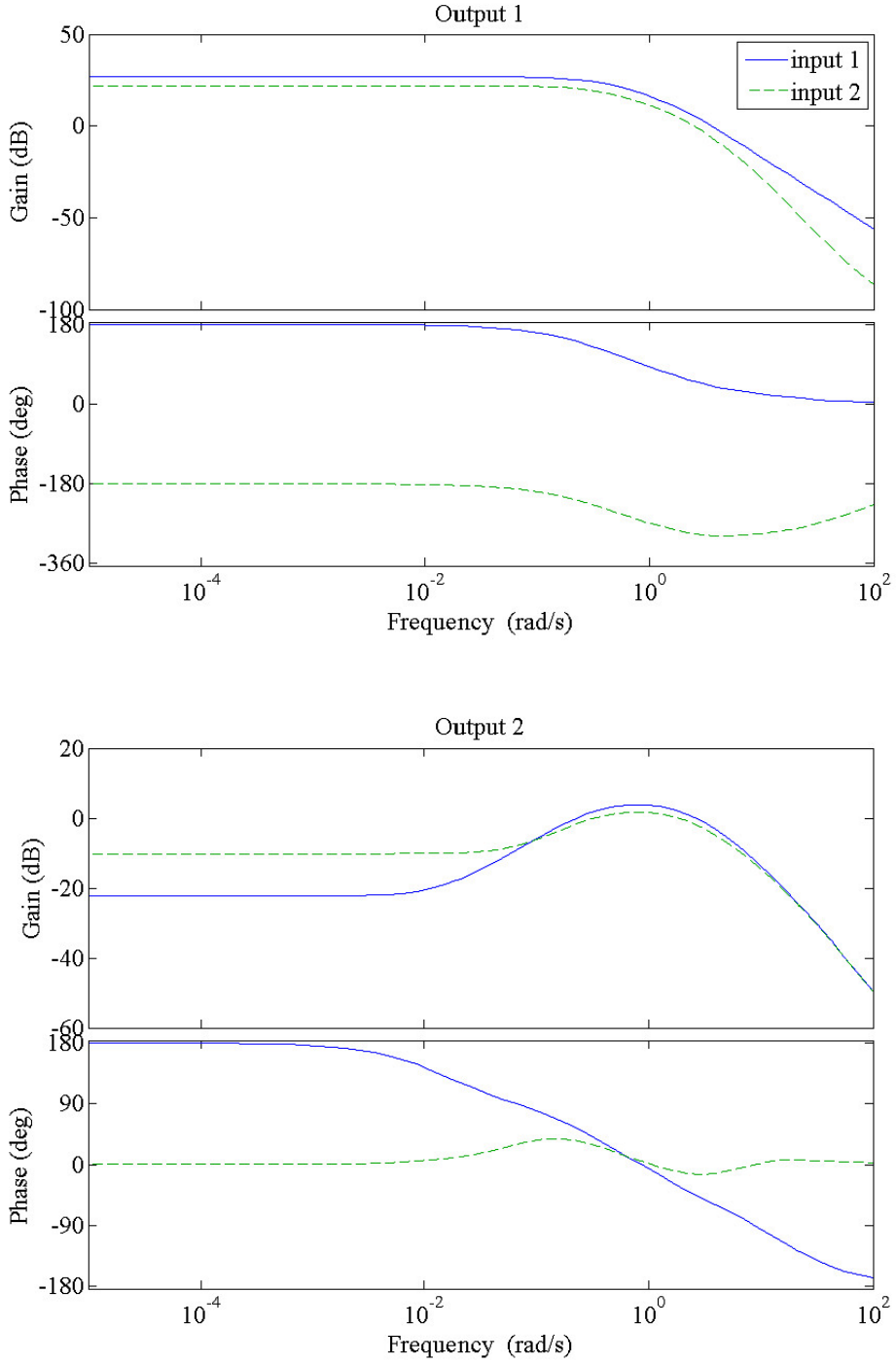

Figure 4: Frequency response for the lumped-mass model

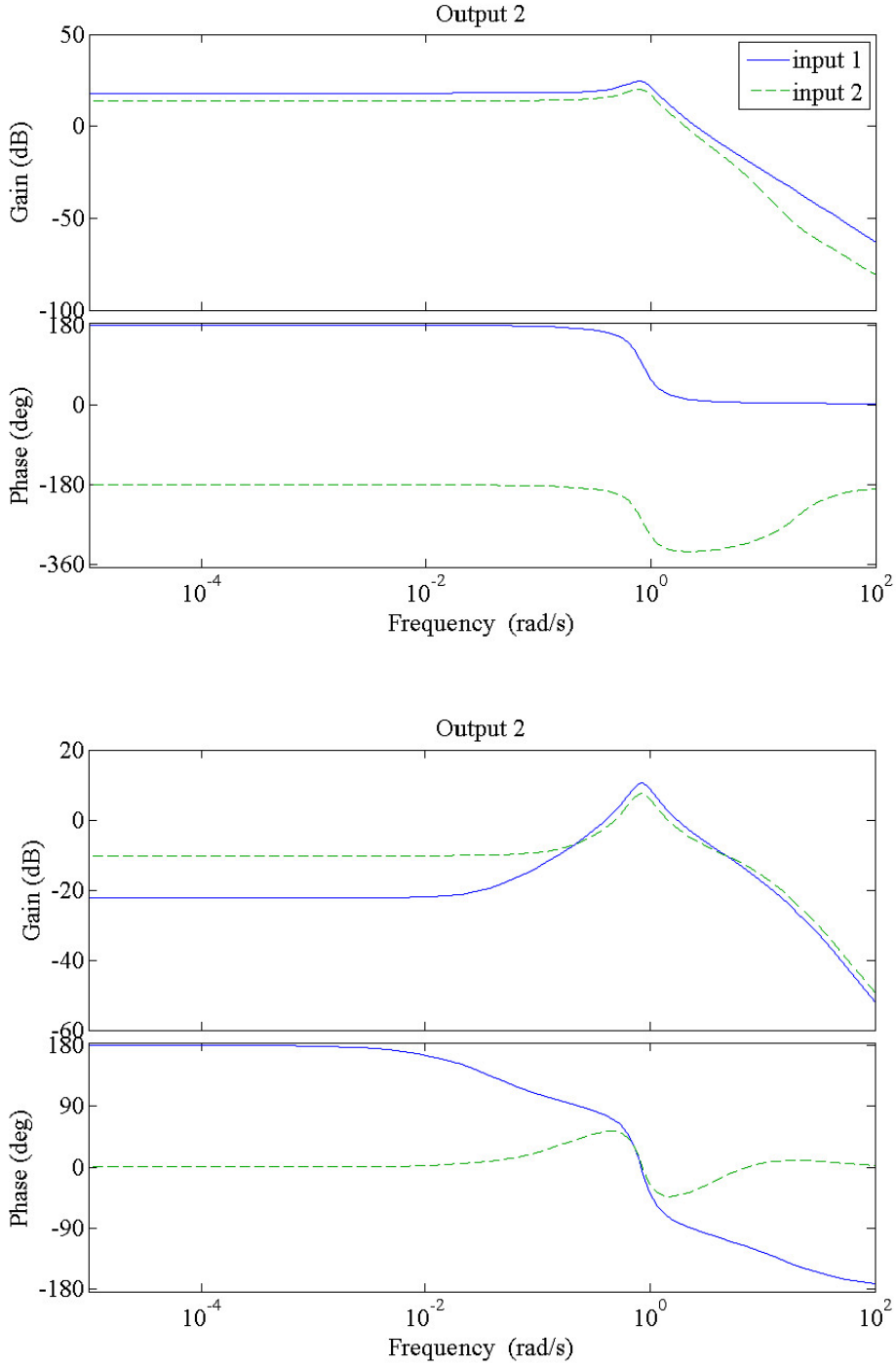

Figure 5: Frequency response for the rigid bar model

4 CONTROL DESIGN

This chapter proposes a control design method to regulate the system to the equilibrium. The method is based on a linear state-feedback control scheme with a nonlinear observer. In this thesis, we present two types of nonlinear observers, one of which is composed of a linear Kalman filter gain and the original state space model, while the other one is based on the concept of high-gain observers [29].

4.1 State-feedback controller

First, we design the state-feedback controller based on the linear system in (38) as shown in Fig. 6. Adopting the linear-quadratic (LQ) optimal control framework, we compute an LQ feedback gain K by MATLAB function "lqr", which minimizes the cost function

$$J = \int_0^\infty (w^T Q w + v^T R v) dt, \tag{48}$$

where Q and R are weighting matrices. We are not eager to determine the best weighting matrices, so the identity matrix is employed for each case. This MATLAB function solves the Riccati equation

$$A^T S + SA - SBR^{-1}B^T S + Q = 0 \tag{49}$$

and provides the LQ gain $K = R^{-1}B^T S$. The LQ gain of the lumped-mass model is

$$K = \begin{bmatrix} -0.4995 & -0.2387 & -2.4332 & 0.4062 \\ 0.6260 & -5.6790 & -15.1800 & -0.9416 \end{bmatrix} \tag{50}$$

and one for the rigid bar model is

$$K = \begin{bmatrix} -0.4574 & 0.6305 & -0.7787 & 0.4345 \\ 0.3934 & -6.0483 & -10.7811 & -0.9489 \end{bmatrix}. \tag{51}$$

Then, control input is given by

$$v = -Kw \tag{52}$$

where $w = x - x^*$. Note that this linear state-feedback controller is based on the linear system in (38), however it successfully regulates the original nonlinear system as demonstrated later.

4.2 Output-feedback controller

Next, to establish an output-feedback controller, we must design an observer to estimate the state of the dynamical system which can recover the performance of the state-feedback controller. In this study, two types of nonlinear observers are constructed and compared with respect to their performances. One approach is composed of the original nonlinear model with a linear Kalman filter gain which is computed for the linear system in (38). This is the natural extension of the linear Kalman filter. The other one utilizes a high-gain observer.

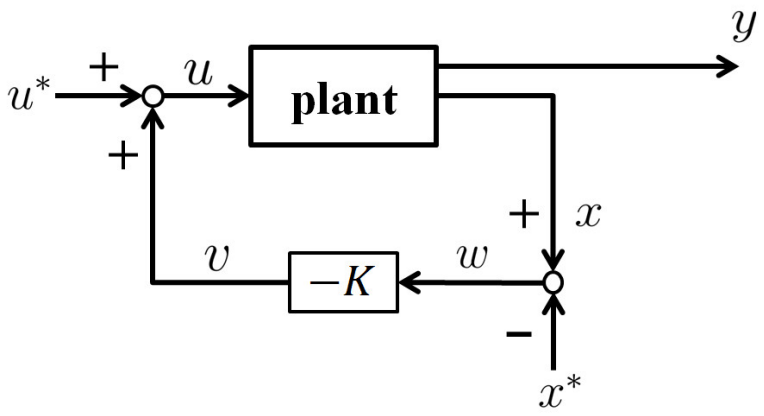

Figure 6: Block diagram of a state-feedback controller

4.2.1 original model with a Kalman filter gain

First, we construct a linear Kalman filter for the linear system in (38) as

$$\dot{\hat{w}} = A\hat{w} + Bv + l(y - C\hat{w}). \tag{53}$$

Employing MATLAB function "kalman", the Riccati equation

$$PA^T + AP - PC^T R_o^{-1} CP + Q_o = 0 \tag{54}$$

is solved, where weighting matrices Q_o and R_o are the identity matrices. Then, combining the resulting Kalman filter gain $l = PC^T R_o^{-1}$ and the original nonlinear system, we obtain a nonlinear observer represented by

$$\dot{\hat{x}} = f(\hat{x}, u) + l(y - \hat{y}) \tag{55}$$

where $\hat{x}$ is an estimated state and $\hat{y} = h(\hat{x}_1)$. Specific value of l for the lumped-mass model is

$$l = \begin{bmatrix} 0.2231 & -0.1576 \\ -2.0587 & 13.2781 \\ 0.4874 & -2.1368 \\ -5.4526 & 90.2736 \end{bmatrix} \tag{56}$$

and

$$l = \begin{bmatrix} 0.3075 & -0.1955 \\ -1.5967 & 15.1803 \\ 0.5423 & -2.7890 \\ -5.4690 & 116.4957 \end{bmatrix} \tag{57}$$

for the rigid bar model. Note that the control input yields

$$v = -K\hat{w}, \tag{58}$$

where $\hat{w} = \hat{x} - x^*$.

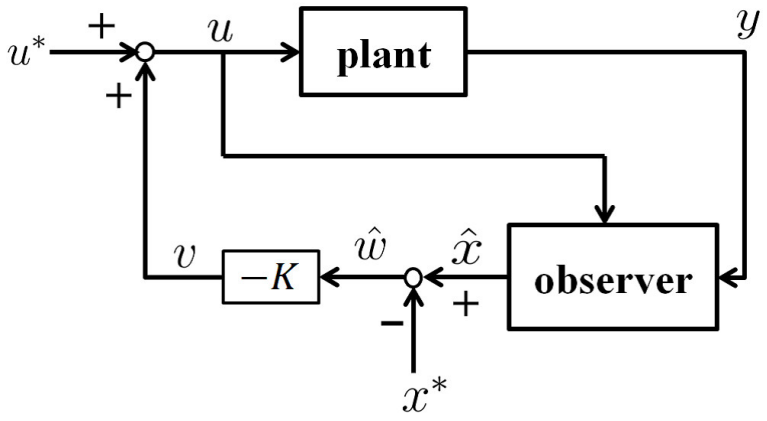

Figure 7: Block diagram of an output-feedback controller

4.2.2 high-gain observer

In order to employ a high-gain observer-based approach we need to apply a coordinate transformation, which is generally utilized in the *input-output linearization* scheme (e.g., see [29]). First, the system (35) can be rewritten in the following form

$$\begin{aligned} \dot{x} &= f'(x) + g(x,u) \\ y &= h(x_1). \end{aligned} \tag{59}$$

Calculating the derivatives of y, we obtain

$$\dot{y} = \begin{bmatrix} -L\dot{x}_{11}\sin(x_{11}) - L_v\dot{x}_{12}\sin(x_{12}) \\ \dot{x}_{12} \end{bmatrix} \tag{60}$$

$$\ddot{y} = H(x) + G(x,u) \tag{61}$$

where $H(x) = L_{f'}^2 h(x)$ and $G(x,u) = L_g L_{f'} h(x)$. $L_{f'}(\cdot)$ and $L_g(\cdot)$ denote the *Lie derivatives* with respect to f' and g. This system has relative degree of two, and by adopting the transformation $z = [z_1^T, z_2^T]^T = [h(x)^T, \dot{h}(x)^T]^T = T(x)$; that is,

$$z = \begin{bmatrix} L\cos(x_{11}) + L_v\cos(x_{12}) \\ x_{12} \\ -L\dot{x}_{11}\sin(x_{11}) - L_v\dot{x}_{12}\sin(x_{12}) \\ \dot{x}_{12} \end{bmatrix}, \tag{62}$$

the system (59) is rewritten as

$$\begin{aligned} \dot{z} &= A_z z + B_z \phi(z,u) \\ y &= C_z z \end{aligned} \tag{63}$$

where $\phi(z,u) = H(T^{-1}(z)) + G(T^{-1}(z),u)$. Each constant matrix is

$$A_z = \begin{bmatrix} 0 & I_2 \\ 0 & 0 \end{bmatrix}, \tag{64}$$

$$B_z = \begin{bmatrix} 0 \\ I_2 \end{bmatrix}, \tag{65}$$

$$C_z = \begin{bmatrix} I_2 & 0 \end{bmatrix}, \tag{66}$$

where I_2 denotes the 2×2 identity matrix.

Finally, by some algebraic manipulation, we can design a high-gain observer as

$$\dot{\hat{z}} = A_z \hat{z} + B_z \phi(\hat{z}, u) + \Gamma(y - C_z \hat{z}) \tag{67}$$

where $\hat{z}$ denotes the estimation of z. Γ is the observer gain such that

$$\Gamma = \begin{bmatrix} \alpha_1/\epsilon & 0 \\ 0 & \alpha_1^2/\epsilon \\ \alpha_2/\epsilon^2 & 0 \\ 0 & \alpha_2^2/\epsilon^2 \end{bmatrix} \tag{68}$$

where positive conatant ϵ is a design parameter. Theoretically, the smaller ϵ leads to the better performance. In addition, we need to set the positive constant α_j^i satisfying that the roots of

$$s^2 + \alpha_1^i s + \alpha_2^i = 0 \tag{69}$$

are located in the open left-half plane ($i = 1, 2$). Note that s denotes the Laplace variable here. We refer to the canonical form of the second order system

$$\ddot{X} + 2\zeta\omega\dot{X} + \omega^2 X = 0 \tag{70}$$

and set the parameters $\zeta = 0.7$ and $\omega = 1$. Then, $\alpha_1 = 1.4$ and $\alpha_2 = 1$ are adopted. Applying the inverse transformation $T^{-1}(\hat{z})$ gives $\hat{x}$ and we can obtain input v in (58).

5 CONTROL SIMULATIONS

In this chapter, control simulations are presented to evaluate designed controllers. We demonstrate regulation performances for given initial deviations from the equilibrium point (i.e., set point) in this thesis. The main aim is to compare performances of the two output-feedback controllers proposed in chapter 4, especially from the viewpoint of how much they can recover the linear state-feedback controller.

5.1 Simulation conditions

As the set point for the output, the depth for the lumped-mass model $y_1^* = 27.21$ (m) and the rigid bar model $y_1^* = 29.07$ m, while the attitude $y_2^* = 0$ (deg) for each case. The initial condition for angular velocity $x_2(0)$ is set to $x_2^* = 0$ (deg/s) for all the cases. On the other hand, for the output-feedback controllers, the initial state estimation is set to the equilibrium of the system, hence $\hat{w}(0) = [0, 0]^T$ for the linear Kalman filter, $\hat{x}(0) = [x_1^{*T}, x_2^{*T}]^T$ for the original system with the linear Kalman filter gain and $\hat{z}(0) = [h(x^*)^T, 0]^T$ for the high-gain observer.

The simulation period for all the cases is 30 s except for the case of the rigid bar model with the output-feedback controller which includes the original model with Kalman gain observer. Moreover, the *dynamic stall* of the wings has to be considered. To strictly model the phenomenon we need to set bounds for the angles of attack α_i, however, for simplicity we restrict the control input u within ± 30 (deg) instead, in this study.

With those conditions, we have performed control simulations for each case by giving various initial deviation of x_1 from the equilibrium x_1^* and explored the maximal initial deviation id_{max}. The procedure of giving initial deviation, proceeding with the next simulation and determining the id_{max} is as in the following.

1. Each case starts with the small absolute value $id = 1.0$ (deg) for the initial condition.

2. Then, taking into account the signs of the deviations, we investigate four cases, $x_1(0) = [\pm id, \pm id]^T$. When the controller can regulate the system successfully for all the deviation case, we proceed to the next simulation by increasing id by 0.1 deg. Otherwise, we proceed to the next one by decreasing id by 0.1 deg.

3. Finally, the maximal id for successful simulations is obtained as the result for each case.

Therefore, the resulting id_{max} for each case can be considered a criterion to evaluate the controller.

Table 2: Results of the Simulations

Case	model	controller (observer)	id_{max} (deg)
C1	lumped-mass	State-Feedback	± 10.5
C2	lumped-mass	linear Kalman filter	± 0.3
C3	lumped-mass	original model with Kalman gain	± 1.4
C4	lumped-mass	high-gain observer ($\epsilon = 0.1$)	± 0.6
C5	lumped-mass	high-gain observer ($\epsilon = 0.01$)	± 3.3
C6	lumped-mass	high-gain observer ($\epsilon = 0.001$)	± 9.6
C7	rigid bar	State-Feedback	± 10.1
C8	rigid bar	linear Kalman filter	± 0.1
C9	rigid bar	original model with Kalman gain	± 1.7
C10	rigid bar	high-gain observer ($\epsilon = 0.1$)	± 0.5
C11	rigid bar	high-gain observer ($\epsilon = 0.01$)	± 4.9
C12	rigid bar	high-gain observer $\epsilon = 0.001$)	± 10.1

5.2 Results and discussion

5.2.1 resulting id_{max}

Table 2 shows the resulting id_{max} for each case; C1 to C6 correspond to the lumped-mass model and C7 to C12 to the rigid bar model. The linear state-feedback case is denoted by C1 and C7. Case C2 and C8 denote the output-feedback controller based on the linear Kalman filter, and the case of the original model with the linear Kalman filter gain is C3 and C9. Regarding the high-gain observer-based controller, we investigate three cases with the design parameter $\epsilon = 0.1$, 0.01, 0.001 (C4-C6 and C10-C12 respectively).

As expected, the state-feedback controllers exhibit the best performance with C1= ± 10.5 (deg) and C7= ± 10.1 deg. For example, the initial condition $x_1^* + [10.5, 10.5]^T = [-15.3117, 10.5]^T$ deg corresponds with the depth of the vehicle $y_1 = 29.14$ m, which is deeper than the set point for the lumped-mass model by around 2 m.

Next, let us compare the output-feedback controllers. As seen from the table, case C2 and C8 show the poorest performance for each model. These results imply the limit of the estimation by a linear observer. While the high-gain observer-based controller with $\epsilon = 0.001$ (C6 and C12) reveals very similar performance to the state-feedback controller. Compared with this, the controller based on the original model with the linear Kalman filter gain (C3 and C7) exhibits poor performance.

5.2.2 simulation examples

Figures 8-30 show some examples of time-series data of the simulations, specifically each output (depth and attitude) and estimation error for output-feedback controllers. Figs. 8-19 correspond to the lumped-mass model and Figs. 20-30 to the rigid bar model. In this thesis, we present $x_1(0) = [+id, +id]^T$ case for all the figures. Note that we prepare two time scale graphs of the estimation error for the high-gain observer-based case C4 to C6 and C10 to C12 to confirm that the estimation error rapidly converges to zero. For instance, see Fig. 13; the top one is for 30 s and the bottom one for 2 s.

Then, let us start with Fig. 11 and Fig. 18. Each case starts with the same initial deviation $x_1(0) = x_1^* + [1.4, 1.4]^T$ deg, which is the id_{max} for C3; that is, $x_1(0) = [-24.4117, 1.4]^T$ deg, $y_1(0) = 27.52$ m. Both of the controllers can regulate the system finally, however their transient performance are obviously different. The result for C3 exhibits unfavorable overshoot while that for C6 does smooth and rapid convergence to the set point. As seen from Fig. 19 and the bottom graph in Fig. 11, this drawback for C3 is due to the poor estimation performance in the transient state.

Further, the similar simulation for the rigid bar model C9 and C12 show more distinct result. As seen from Fig. 22, Fig. 29 and Fig. 30, which start the id_{max} for C9 $x_1(0) = [-14.1005, 1.7]^T$ deg, case C9 exhibits the vibrational behavior and requires more time to converge (60 s). Note that such kind of behavior is observed only in this case.

Next, it is also seen from the Table 2 that the choice of ϵ is strongly influential to the resulting controller performance for the high-gain observer-based approach. Figs. 12-15 or Figs. 23-26 are positive examples. We compare the results of the high-gain observes between $\epsilon = 0.1$ and $\epsilon = 0.01$ here. In these cases, not only the maximal id become large, but transient performance also improved and the time for convergence of the estimation error shortens.

Finally, let us see Fig. 9 and Fig. 16, here we compare the state-feedback controller C1 and the high-gain observer C6 with $\epsilon = 0.001$. Their initial condition is $x_1(0) = [-16.2100, 9.6]^T$ deg and we can recognize that the high-gain observer recovers the performance of the state-feedback controller. Moreover, the similar comparison for the rigid bar model C7 (Fig. 20) and C12 (Fig. 27) show more desirable results; the high-gain observer shows the same id_{max} with the state-feedback controller. They start with the identical initial condition of $x_1(0) = [-5.6993, 10.1]^T$ deg, which means that $y_1(0) = 30.05$ m.

As seen from the result of all mentioned above, it is obvious that the high-gain observer-based controller can achieve better performance than the other nonlinear output-feedback controller and is easy to design by only modifying the parameter ϵ for such a complex nonlinear system. Note that the controller with $\epsilon = 0.0001$ reveals almost the same results as that of the one $\epsilon = 0.001$. Hence, we can conclude that $\epsilon = 0.001$ is the best parameter for the present problem.

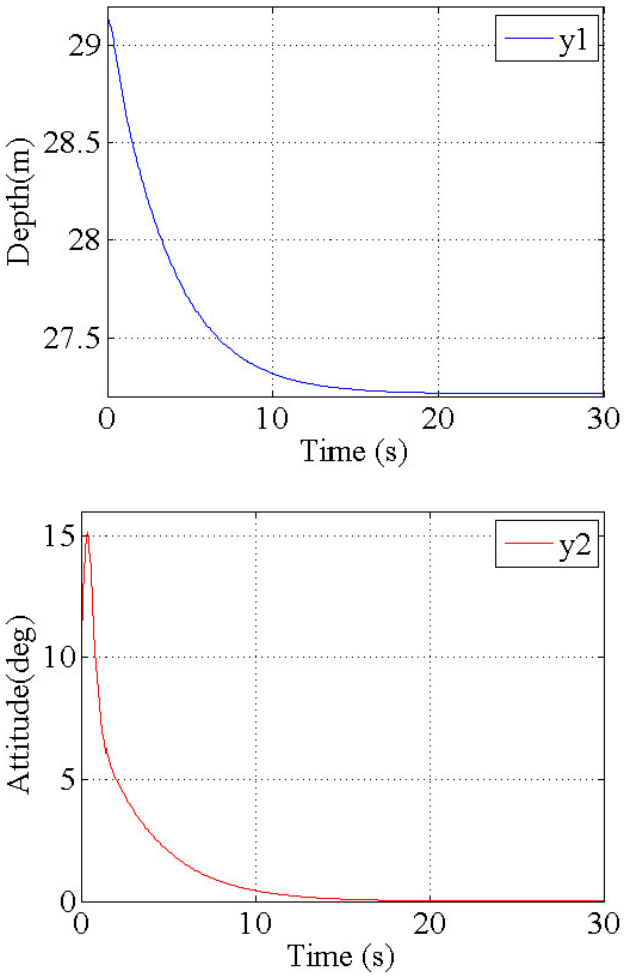

Figure 8: Simulation results in C1 : lumped-mass model and state-feedback controller with $x(0) - x^* = [10.5, 10.5, 0, 0]^T$; deviations from y^*. y_1 is the depth of the vehicle and y_2 is the attitude of the vehicle.

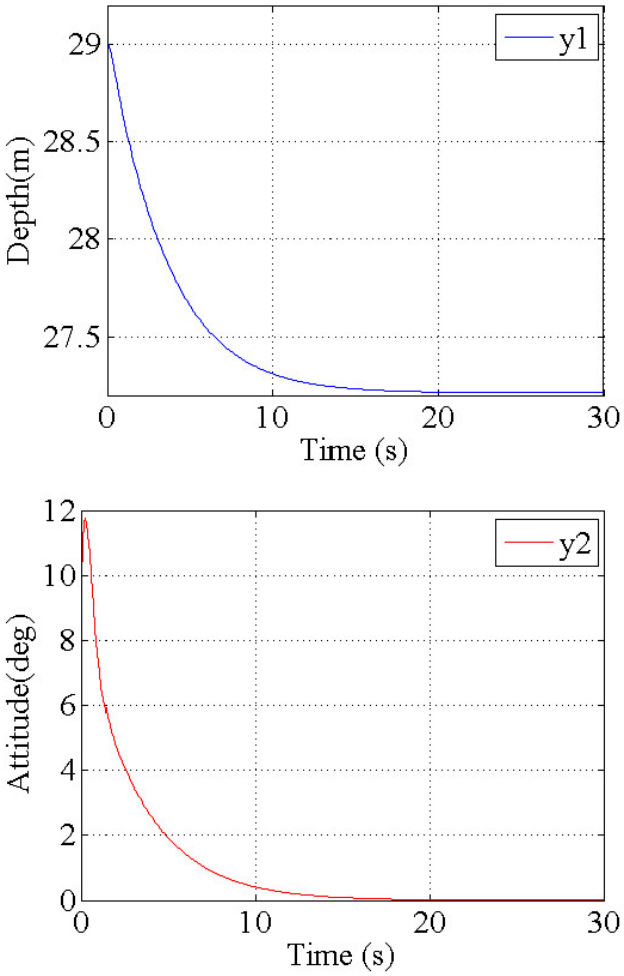

Figure 9: Simulation results in C1 : lumped-mass model and state-feedback controller with $x(0) - x^* = [9.6, 9.6, 0, 0]^T$; deviations from y^*. y_1 is the depth of the vehicle and y_2 is the attitude of the vehicle.

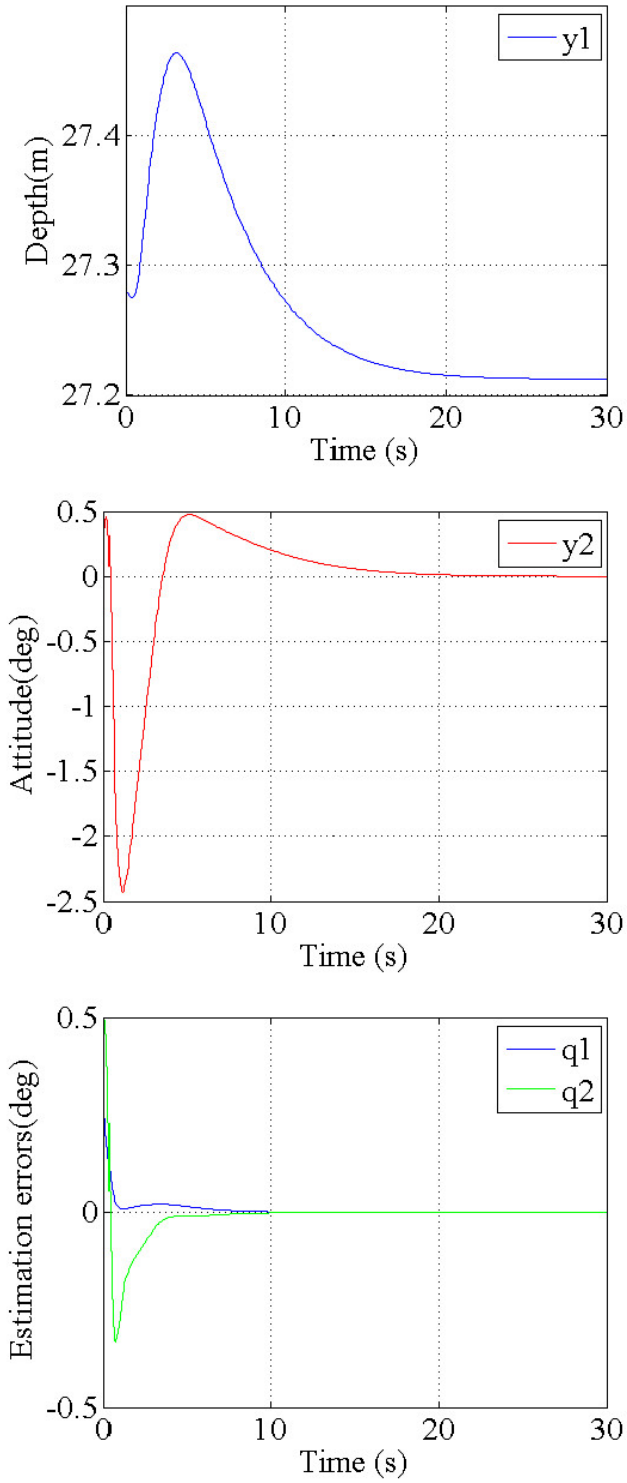

Figure 10: Simulation results in C2 : lumped-mass model and linear Kalman filter with $x(0) - x^* = [0.3, 0.3, 0, 0]^T$; deviations from y^* and estimation errors. y_1 is the depth of the vehicle and y_2 is the attitude of the vehicle. q_1 is the angle of the cable and q_2 is the angle of the vehicle.

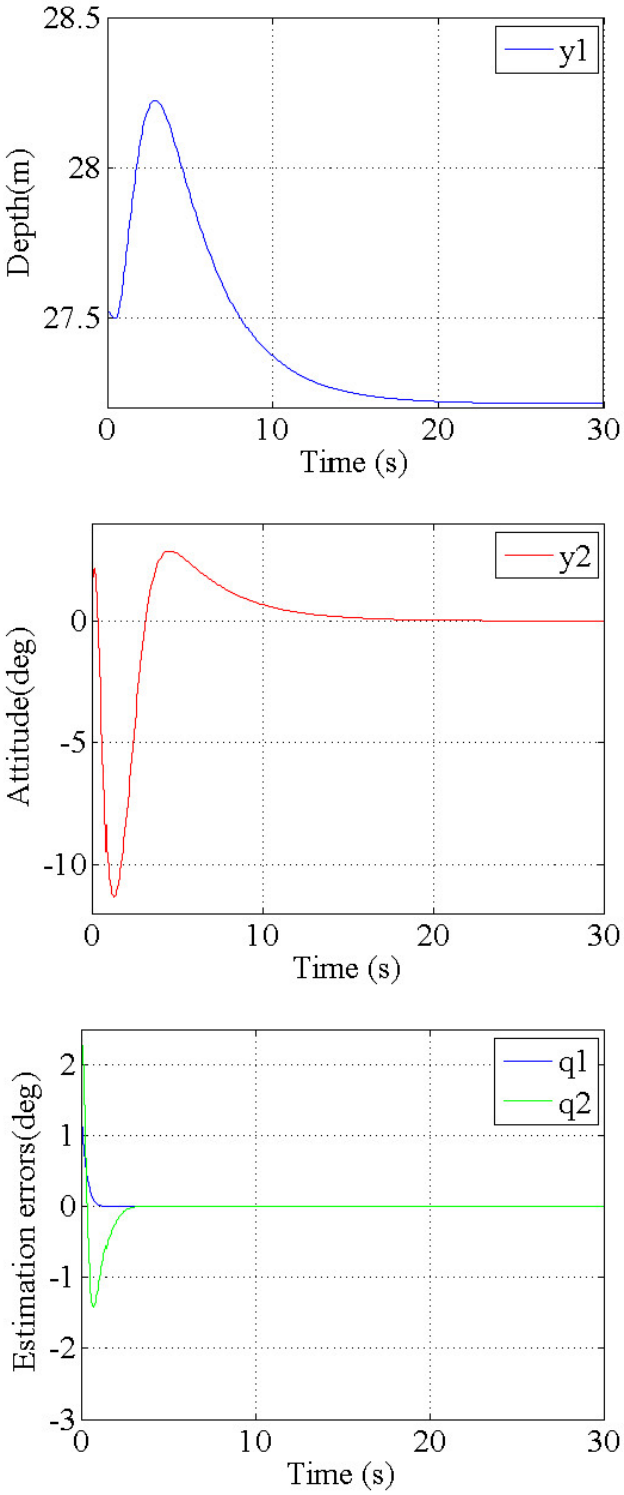

Figure 11: Simulation results in C3 : lumped-mass model and original model with Kalman gain observer with $x(0) - x^* = [1.4, 1.4, 0, 0]^T$; deviations from y^* and estimation errors. y_1 is the depth of the vehicle and y_2 is the attitude of the vehicle. q_1 is the angle of the cable and q_2 is the angle of the vehicle.

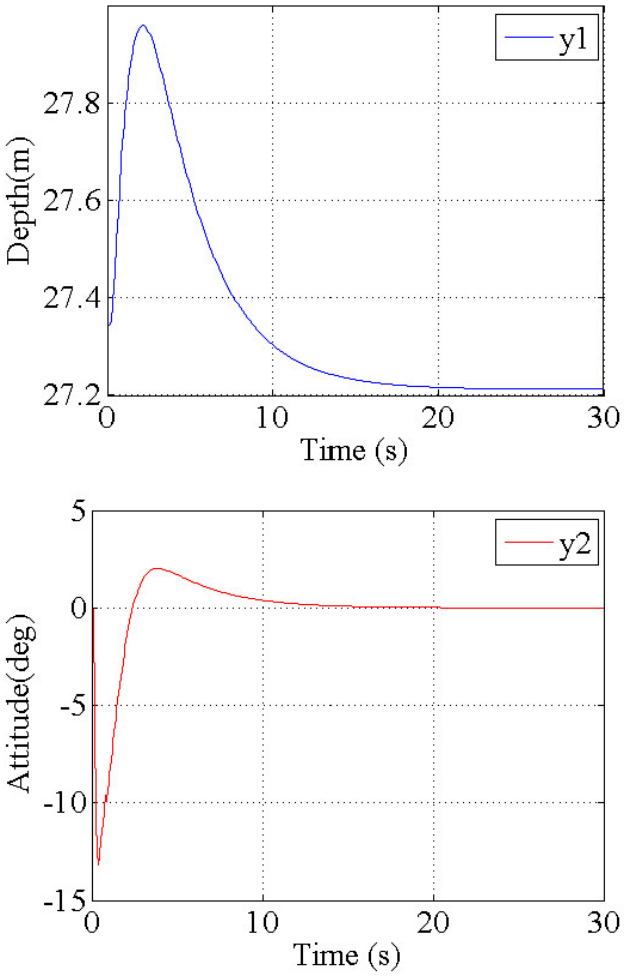

Figure 12: Simulation results in C4 : lumped-mass model and high-gain observer ($\epsilon = 0.1$) with $x(0) - x^* = [0.6, 0.6, 0, 0]^T$; deviations from y^*. y_1 is the depth of the vehicle and y_2 is the attitude of the vehicle.

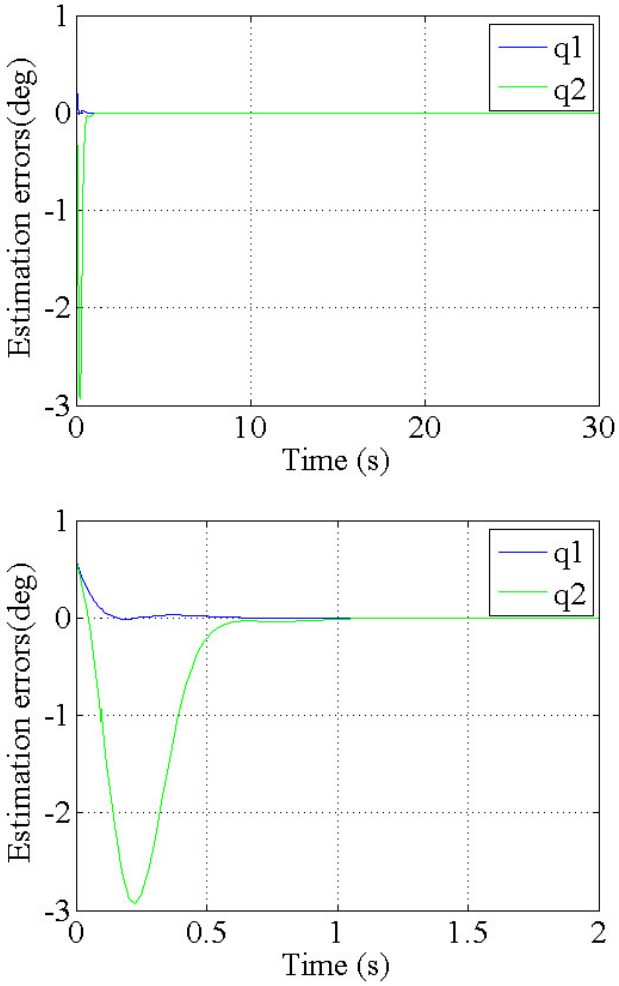

Figure 13: Simulation results in C4 : lumped-mass model and high-gain observer ($\epsilon = 0.1$) with $x(0) - x^* = [0.6, 0.6, 0, 0]^T$; estimation errors. The top one is for 30 s and the bottom one for 2 s. q_1 is the angle of the cable and q_2 is the angle of the vehicle.

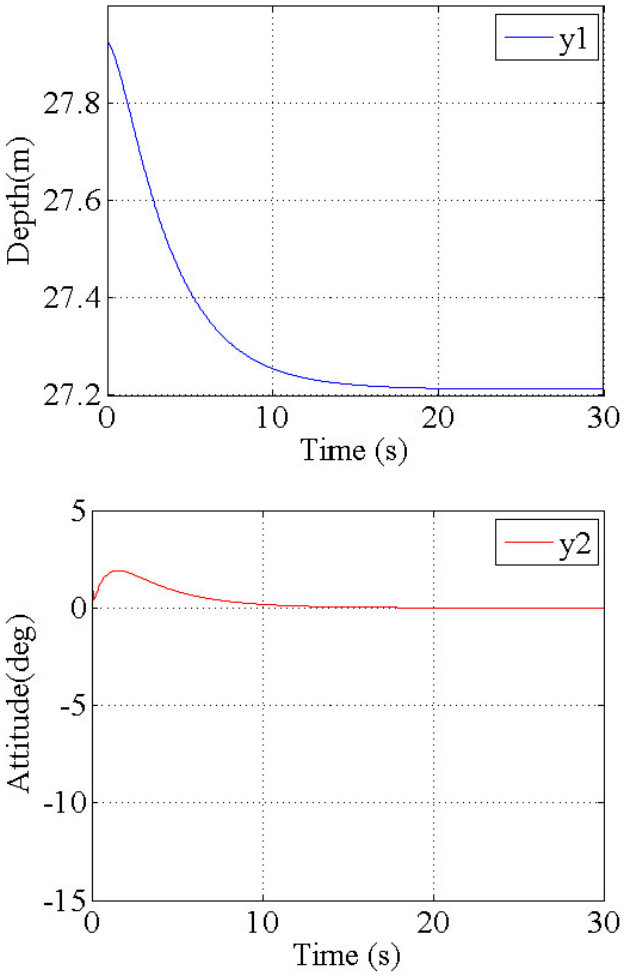

Figure 14: Simulation results in C5 : lumped-mass model and high-gain observer ($\epsilon = 0.01$) with $x(0) - x^* = [3.3, 3.3, 0, 0]^T$; deviations from y^*. y_1 is the depth of the vehicle and y_2 is the attitude of the vehicle.

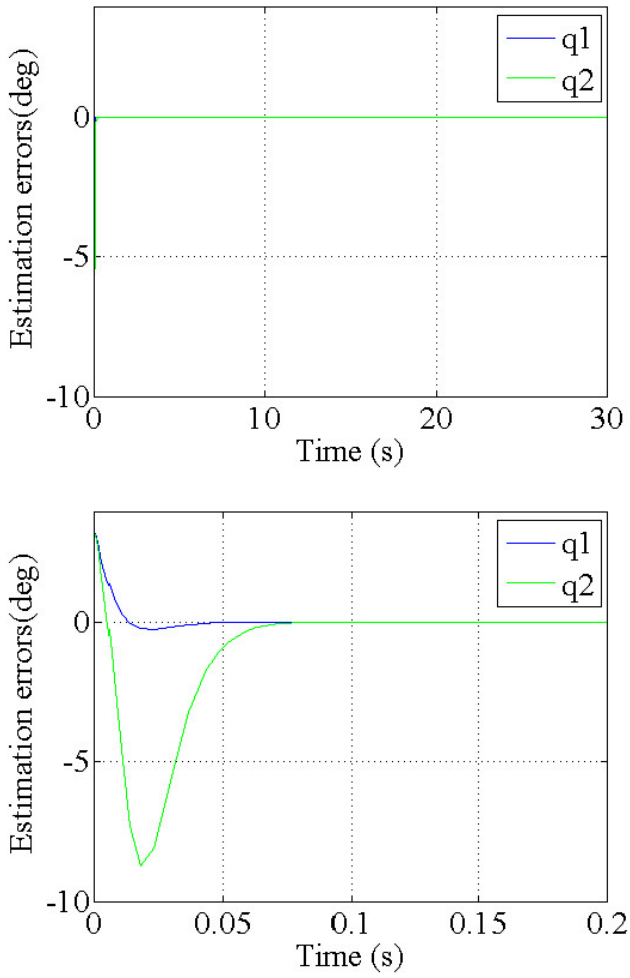

Figure 15: Simulation results in C5 : lumped-mass model and high-gain observer ($\epsilon = 0.01$) with $x(0) - x^* = [3.3, 3.3, 0, 0]^T$; estimation errors. The top one is for 30 s and the bottom one for 0.2 s. q_1 is the angle of the cable and q_2 is the angle of the vehicle.

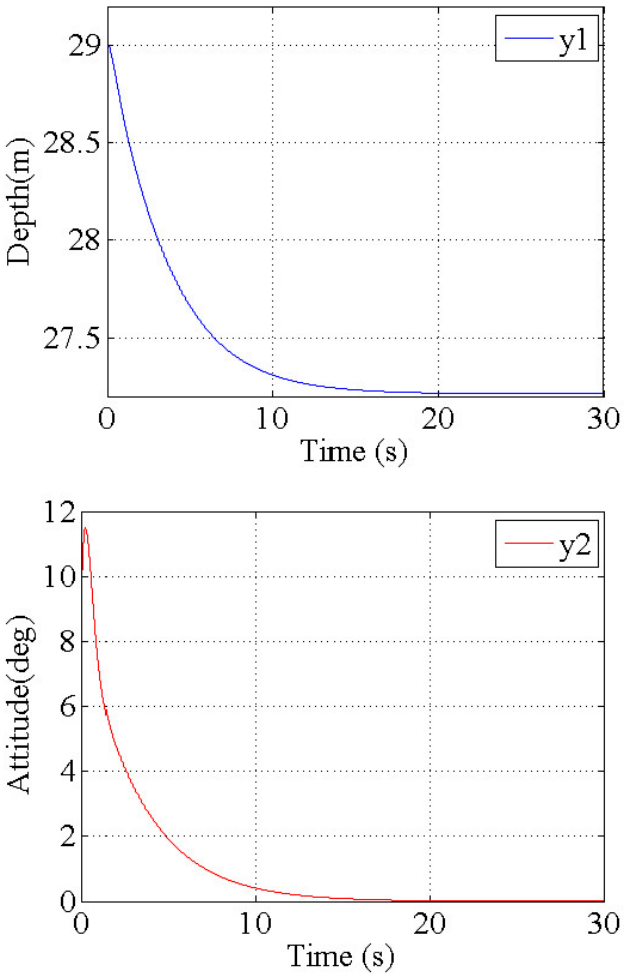

Figure 16: Simulation results in C6 : lumped-mass model and high-gain observer ($\epsilon = 0.001$) with $x(0) - x^* = [9.6, 9.6, 0, 0]^T$; deviations from y^*. y_1 is the depth of the vehicle and y_2 is the attitude of the vehicle.

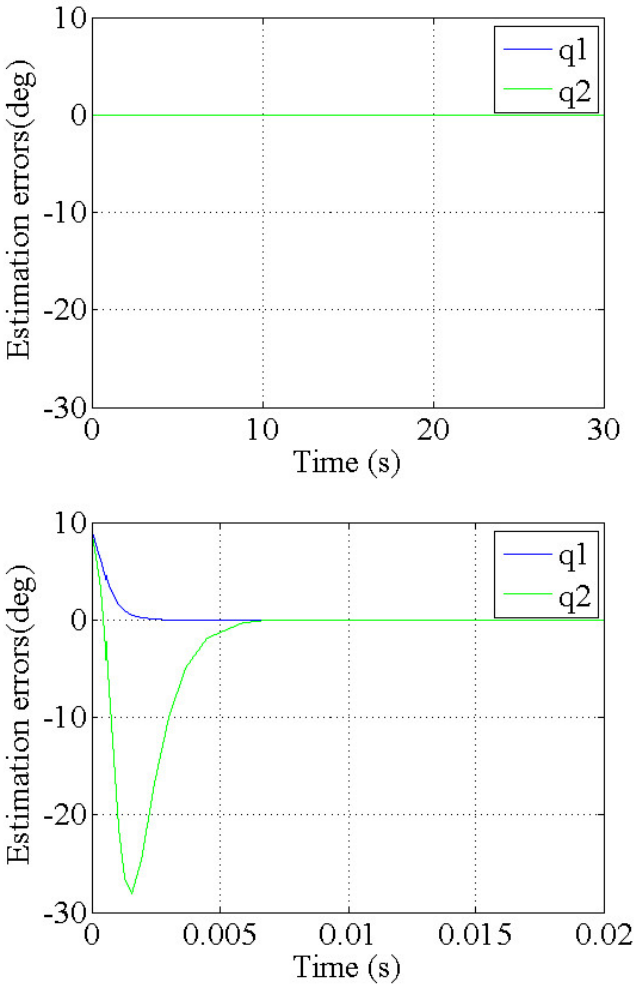

Figure 17: Simulation results in C6 : lumped-mass model and high-gain observer ($\epsilon = 0.001$) with $x(0) - x^* = [9.6, 9.6, 0, 0]^T$; estimation errors. The top one is for 30 s and the bottom one for 0.02 s. q_1 is the angle of the cable and q_2 is the angle of the vehicle.

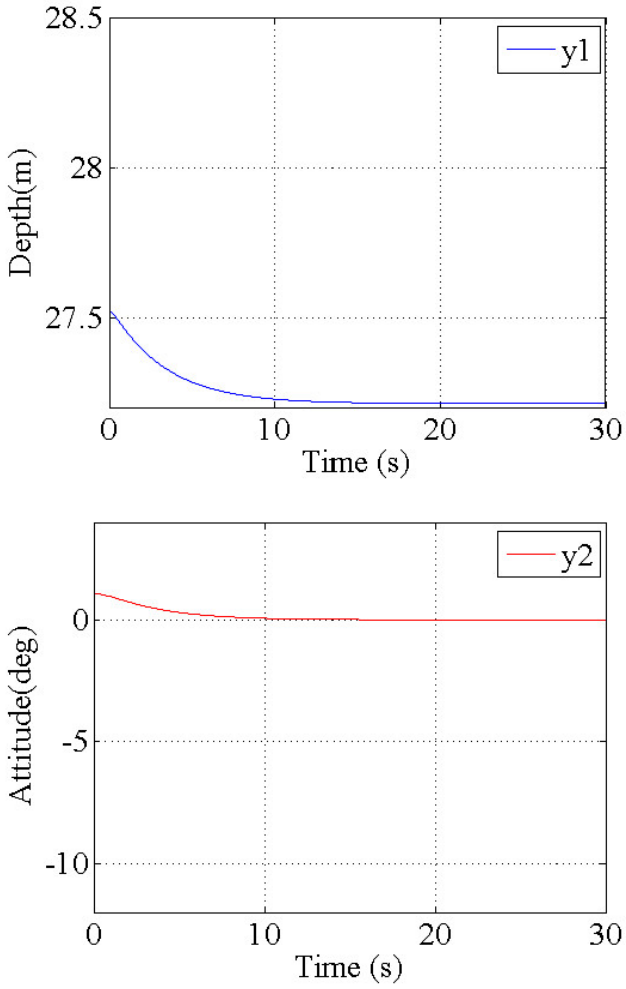

Figure 18: Simulation results in C6 : lumped-mass model and high-gain observer ($\epsilon = 0.001$) with $x(0) - x^* = [1.4, 1.4, 0, 0]^T$; deviations from y^*. y_1 is the depth of the vehicle and y_2 is the attitude of the vehicle.

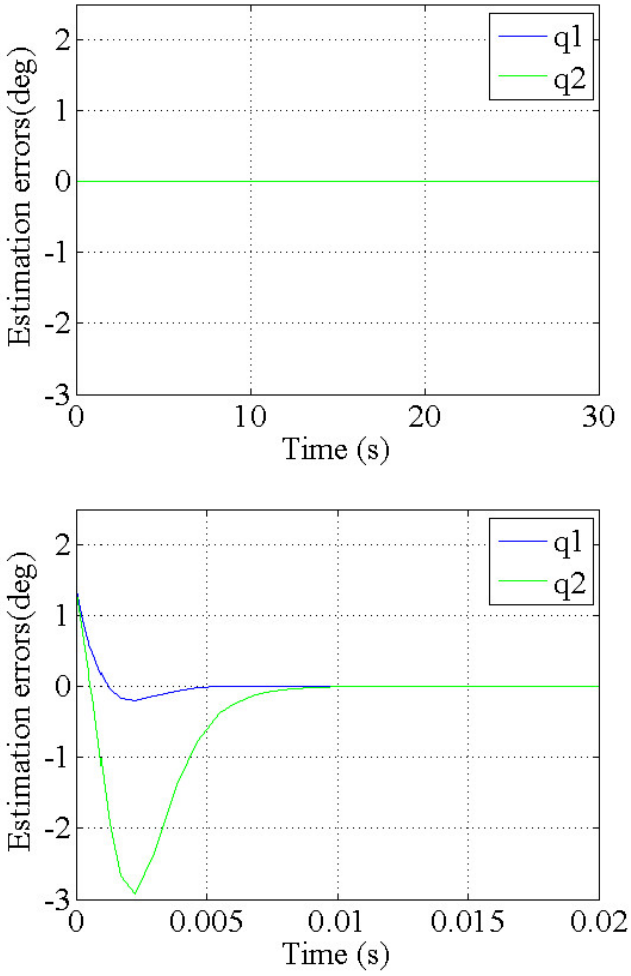

Figure 19: Simulation results in C6 : lumped-mass model and high-gain observer ($\epsilon = 0.001$) with $x(0) - x^* = [1.4, 1.4, 0, 0]^T$; estimation errors. The top one is for 30 s and the bottom one for 0.02 s. q_1 is the angle of the cable and q_2 is the angle of the vehicle.

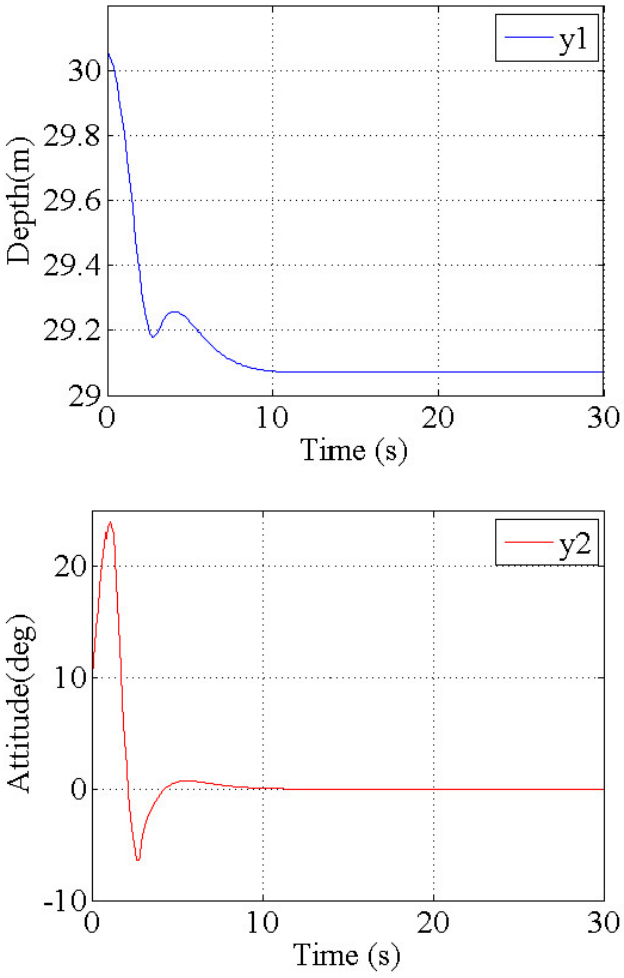

Figure 20: Simulation results in C7 : rigid bar model and state-feedback controller with $x(0) - x^* = [10.1, 10.1, 0, 0]^T$; deviations from y^*. y_1 is the depth of the vehicle and y_2 is the attitude of the vehicle.

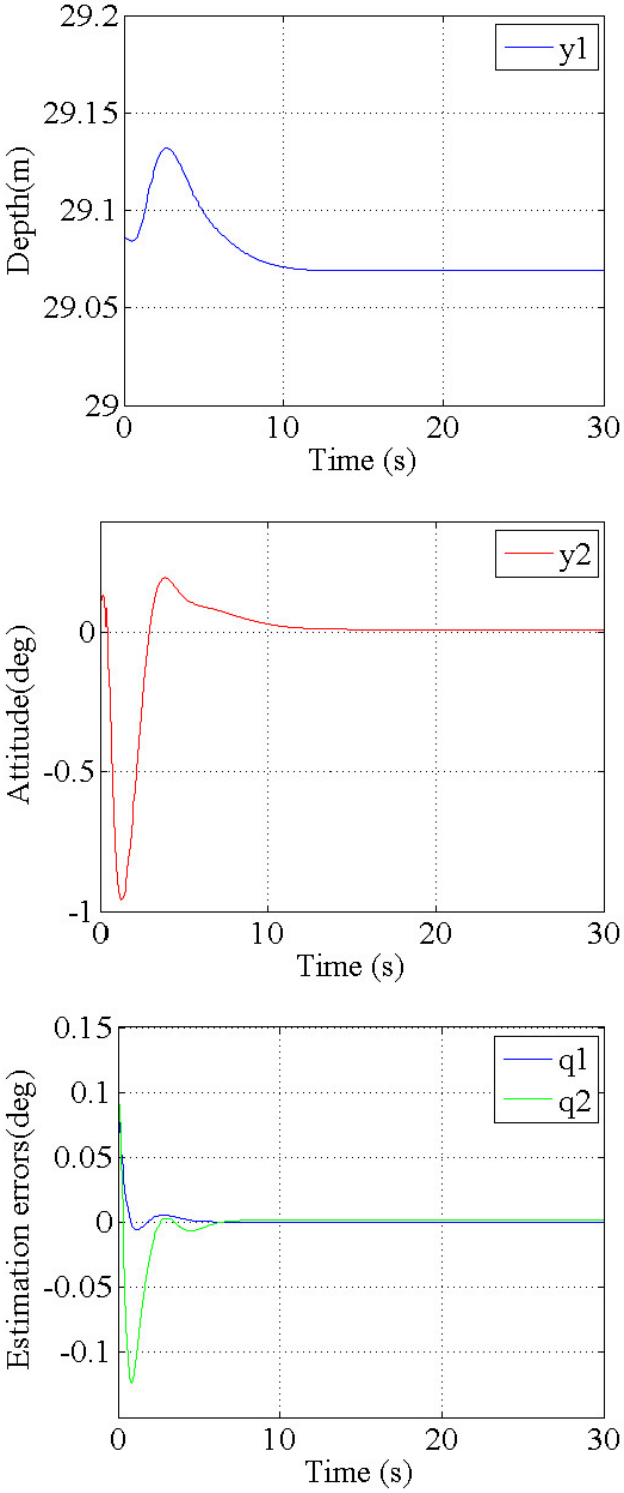

Figure 21: Simulation results in C8 : rigid bar and linear Kalman filter with $x(0) - x^* = [0.1, 0.1, 0, 0]^T$; deviations from y^* and estimation errors. y_1 is the depth of the vehicle and y_2 is the attitude of the vehicle. q_1 is the angle of the cable and q_2 is the angle of the vehicle.

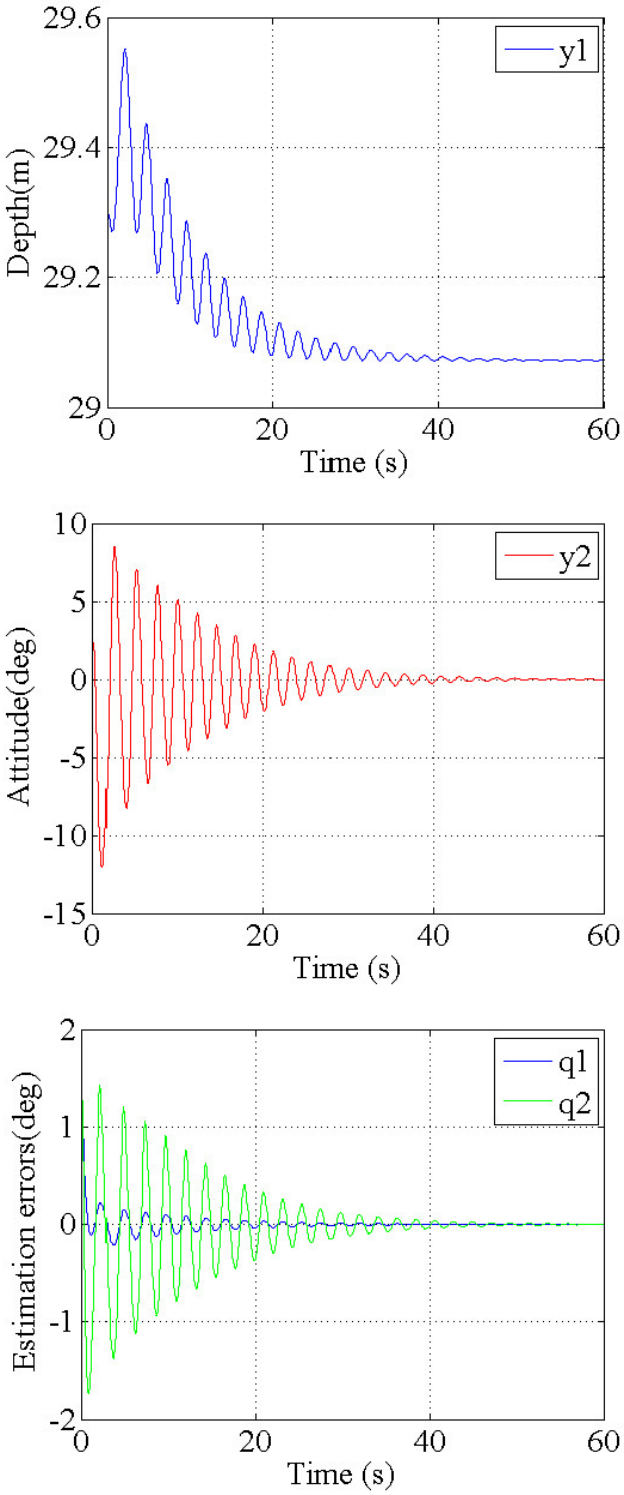

Figure 22: Simulation results in C9 : rigid bar and original model with Kalman gain observer with $x(0) - x^* = [1.7, 1.7, 0, 0]^T$; deviations from y^* and estimation errors. y_1 is the depth of the vehicle and y_2 is the attitude of the vehicle. q_1 is the angle of the cable and q_2 is the angle of the vehicle.

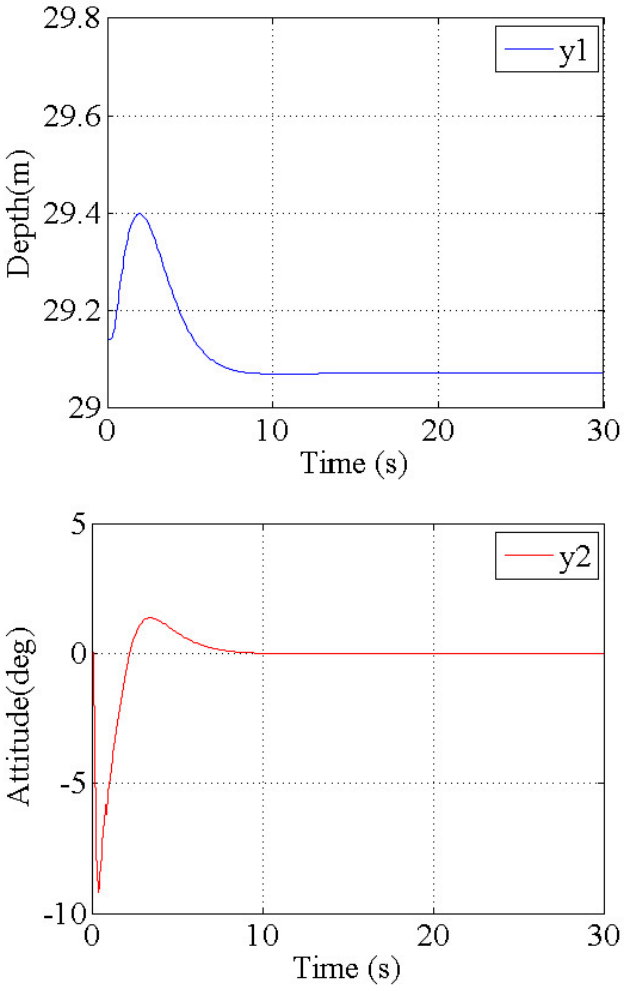

Figure 23: Simulation results in C10 : rigid bar and high-gain observer ($\epsilon = 0.1$) with $x(0) - x^* = [0.5, 0.5, 0, 0]^T$; deviations from y^*. y_1 is the depth of the vehicle and y_2 is the attitude of the vehicle.

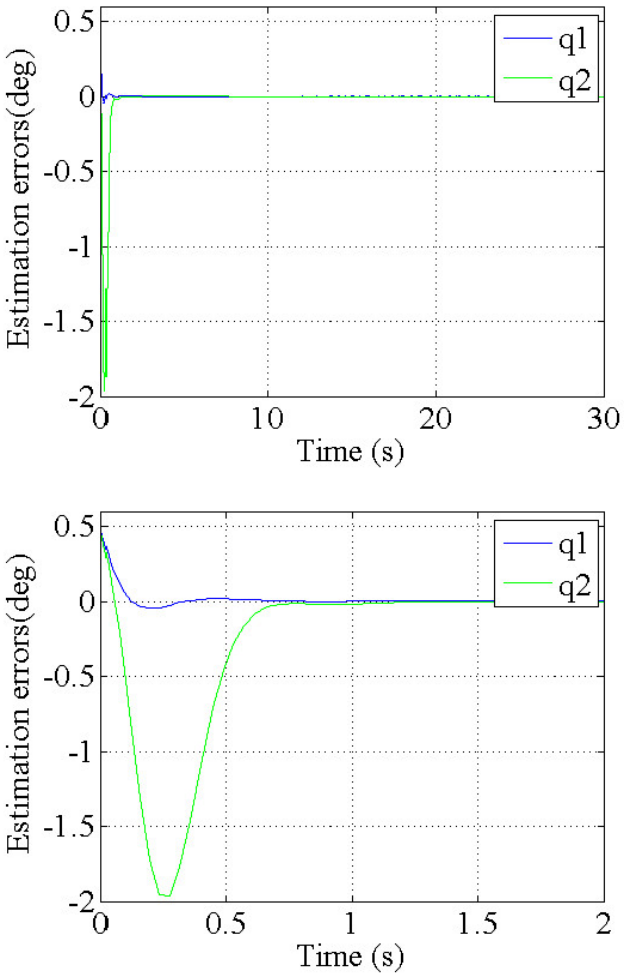

Figure 24: Simulation results in C10 : rigid bar and high-gain observer ($\epsilon = 0.1$) with $x(0) - x^* = [0.5, 0.5, 0, 0]^T$; estimation errors. The top one is for 30s and the bottom one for 2s. q_1 is the angle of the cable and q_2 is the angle of the vehicle.

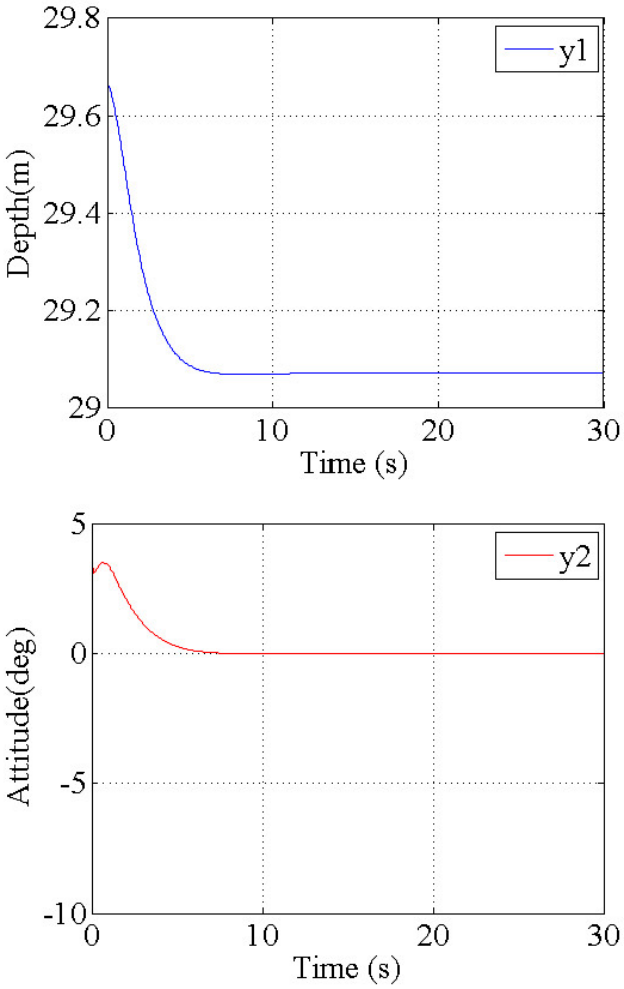

Figure 25: Simulation results in C11 : rigid bar and high-gain observer ($\epsilon = 0.01$) with $x(0) - x^* = [4.9, 4.9, 0, 0]^T$; deviations from y^*. y_1 is the depth of the vehicle and y_2 is the attitude of the vehicle.

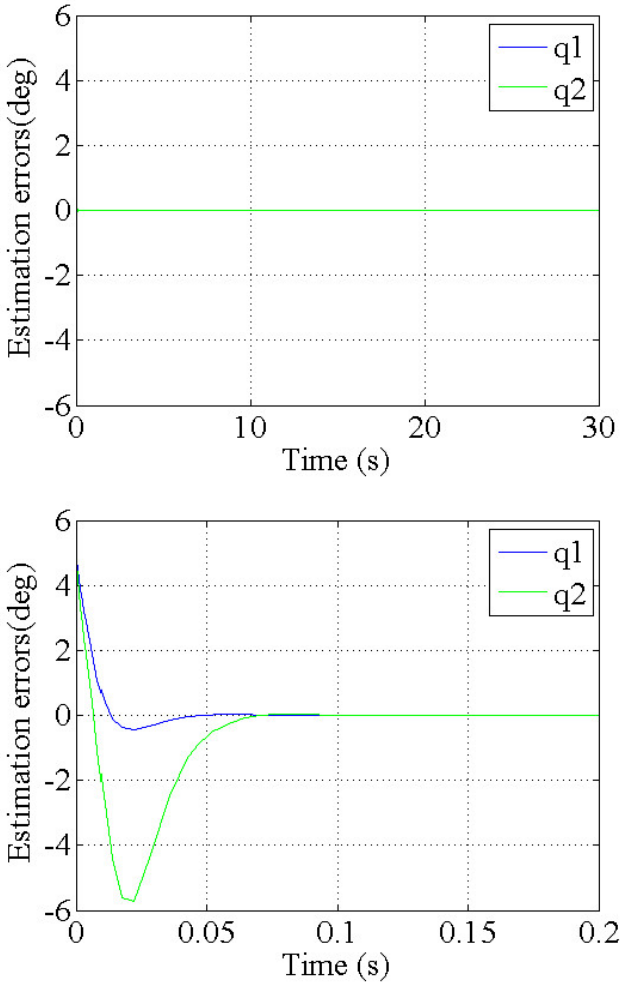

Figure 26: Simulation results in C11 : rigid bar and high-gain observer ($\epsilon = 0.01$) with $x(0) - x^* = [4.9, 4.9, 0, 0]^T$; estimation errors. The top one is for 30s and the bottom one for 0.2s. q_1 is the angle of the cable and q_2 is the angle of the vehicle.

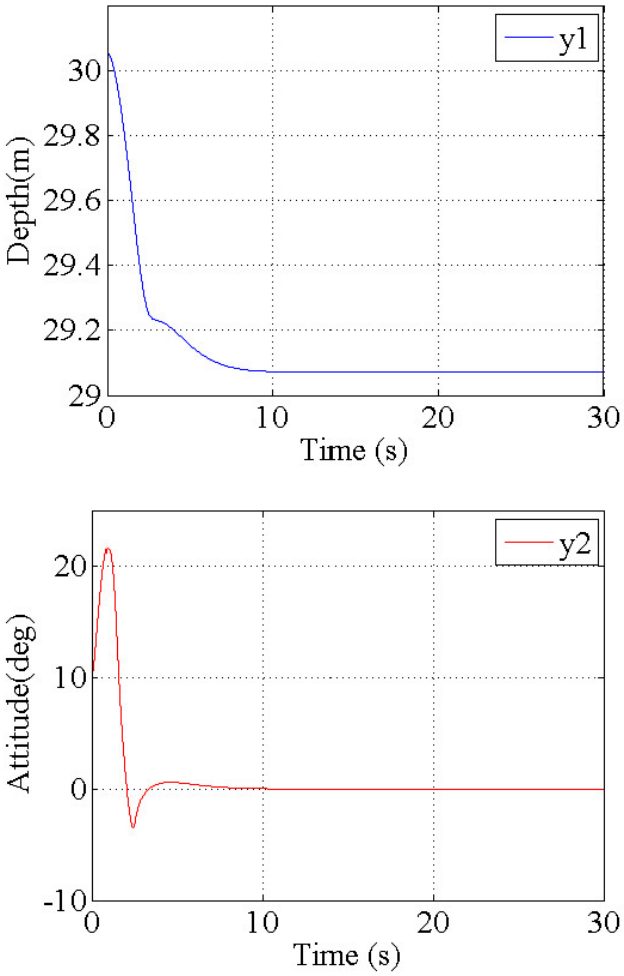

Figure 27: Simulation results in C12 : rigid bar and high-gain observer ($\epsilon = 0.001$) with $x(0) - x^* = [10.1, 10.1, 0, 0]^T$; deviations from y^*. y_1 is the depth of the vehicle and y_2 is the attitude of the vehicle.

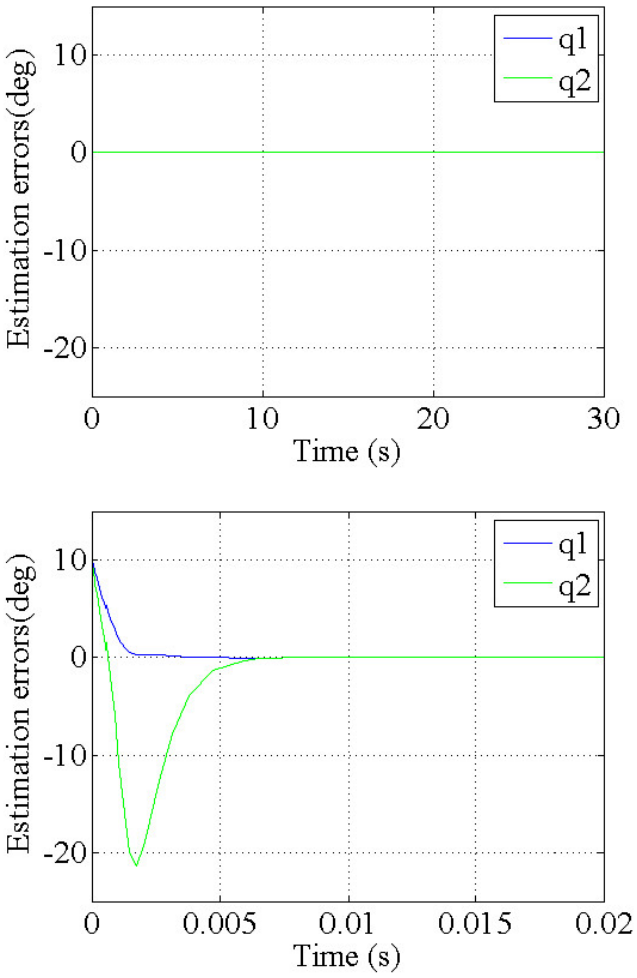

Figure 28: Simulation results in C12 : rigid bar and high-gain observer ($\epsilon = 0.001$) with $x(0) - x^* = [10.1, 10.1, 0, 0]^T$; estimation errors. The top one is for 30 s and the bottom one for 0.02 s. q_1 is the angle of the cable and q_2 is the angle of the vehicle.

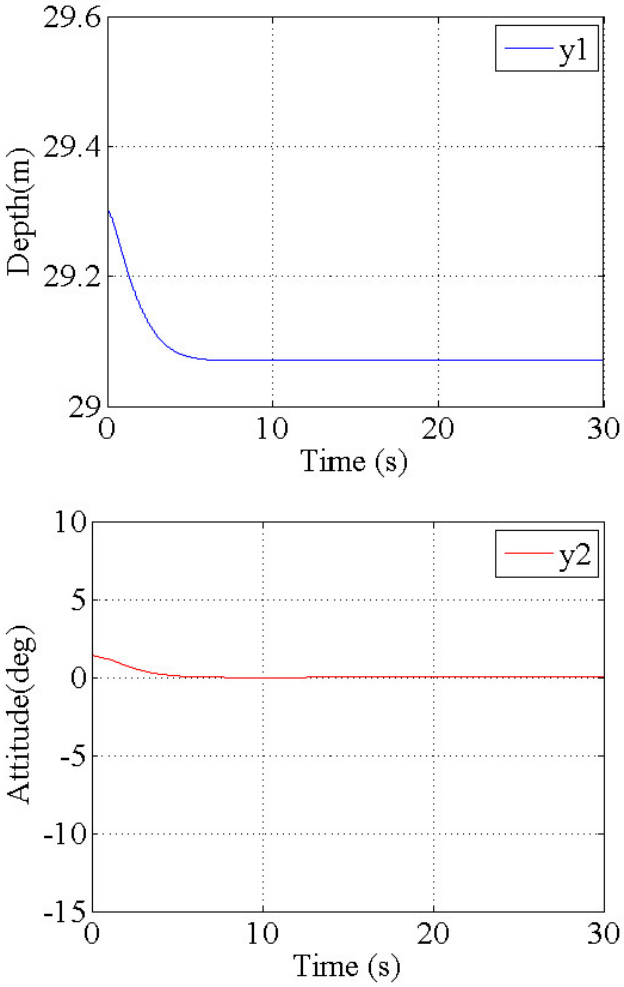

Figure 29: Simulation results in C12 : rigid bar and high-gain observer ($\epsilon = 0.001$) with $x(0) - x^* = [1.7, 1.7, 0, 0]^T$; deviations from y^*. y_1 is the depth of the vehicle and y_2 is the attitude of the vehicle.

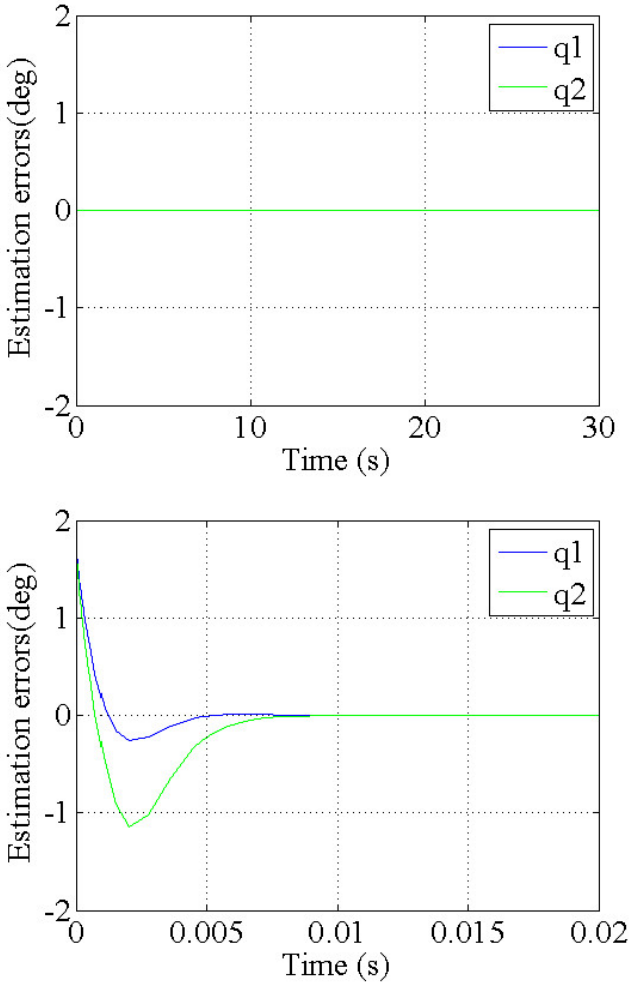

Figure 30: Simulation results in C12 : rigid bar and high-gain observer ($\epsilon = 0.001$) with $x(0) - x^* = [1.7, 1.7, 0, 0]^T$; estimation errors. The top one is for 30 s and the bottom one for 0.02 s. q_1 is the angle of the cable and q_2 is the angle of the vehicle.

6 CONCLUSIONS AND FUTURE WORK

In this thesis, we have addressed the depth and attitude control problem of a TUV with movable wings. First, two types of the dynamical model, the lumped-mass model in the lowest-order case and the rigid bar case have been given. Second, some basic characteristics of the system such as stability, controllability and observability have been analyzed and we have verified that a stabilizing control system based on state-feedback controllers and observers could be designed. Then two types of output-feedback controllers have been designed; the one of the controllers is based on the concept of high-gain observers, and the other one consists of the original model with a linear Kalman filter gain. In order to evaluate their regulation performances, some simulations have been conducted. According to the simulation results, the output-feedback controller with the high-gain observer have performed much better than the other controller, and is easy to design by only modifying the parameter ϵ. Then, we have concluded that the high-gain observer-based approach is feasible and effective for such TUVs.

In the end, we give some research directions for future work. At first, we would like to expand the control law for tracking such that the output y asymptotically tracks a reference signal. In this thesis position-fixed controllers are designed, however a control target, particularly the depth of the vehicle often alters in practical operations. Next, we will proceed to the dynamical model in higher-order case, and some assumptions will be changed especially the dynamics of the environmental water current will be taken into consideration. These modifications are necessary to develop an active control system, which guarantees observations of a TUV with higher accuracy. In addition, we wish to investigate the robustness of the control system in the future.

References

[1] J.K.Cochran, "Oceanographic Sampling and Measurements," Elsevier Reference Module in Earth Systems and Environmental Sciences, pp, 1-7, 2014.

[2] C.Albaladejo, F.Soto, R.Torres, P.Sanchez, J.A.Lopez, "A Low-Cost Seneor Buoy System for Monitoring Shallow Marine Environments," Sensors, 12, pp, 9613-9634, 2012.

[3] S.Kroger, R.J.Law, "Sensing the sea," Trends in Biotechnology, 23, no. 5, pp, 250-256, 2005.

[4] D.Roemmich, G.C.Johnson, S.Riser, R.Davis, J.Gilson, W.B.Owens, S.L.Garzoli, C.Schmid, M.Ignaszewski, "The Argo Program: Observing the global ocean with profiling floats," Oceanography, 22, pp, 34-43, 2009.

[5] M.A.Tivey, H.P.Johnson, A.Bradly, D.Yoerger, "Thickness of a submarine lava flow determined from near-bottom magnetic field mapping by autonomous underwater vehicle," Geophysical research letters, vol. 25, no. 6, pp, 805-808, 1998.

[6] G.Griffiths, "Step towards autonomy: From current measurements to underwater vehicles," Methods in Oceanography, 1-2, pp, 22-48, 2012.

[7] E.Bovio, D.Cecchi, F.Baralli, "Autonomous underwater vahicles for scientific and naval operations," Annual Reviews in Control, 30, pp, 117-130, 2006.

[8] K.Alam, T.Ray, S.G.Anavatti, "A brief taxonomy of autonomous underwater vehicle design literature," Ocean Engineering, 88, pp, 627-630, 2014.

[9] R.B.Wynn, V.A.I.Huvenne, T.P.Le Bas, B.J.Murton, D.P.Connelly, B.J.Bett, H.A.Ruhl, K.J.Morris, J.Peakall, D.R.Parsons, E.J.Sumner, S.E.Darby, R.M.Dorrell, J.E.Hunt, "Autonomous underwater vehicles (AUVs):Their past, present and future contributions to the advancement of marine geoscience," Marine Geology, 352, pp, 451-468, 2014.

[10] M.Marcelli, V.Piermattei, A.Madonia, U.Mainardi, "Design and Application of New Low-Cost Instruments for Marine Environmental Research," Sensors, 14, pp, 23348-23364, 2014.

[11] X.Wang, J.Shang, Z.Luo, L.Tang, X.Zhang, J.Li, "Reviews of power systems and environmental energy conversion for unmanned underwater vehicles," Renewable and Sustainable Energy Reviews, vol. 16, no. 4, pp, 1958-1970, 2012.

[12] T.Yokobiki, W.Koterayama, S. Yamaguchi and M. Nakamura, "Dynamics and control of a towed vehicle in transient mode," Int. J. of Offshore and Polar Engineering, vol. 1, pp. 19-25, 2000.

[13] B.Buckham, M.Nahon, M.Seto, X.Zhao and C.Lambert, "Dynamics and control of a towed underwater vehicle system, part I: model development," Ocean Engineering, 30, pp, 453-470, 2003.

[14] C.Lambert, M.Nahon, B.Buckham and M.Seto "Dynamics and control of a towed underwater vehicle system, part II: model validation and turn maneuver optimization," Ocean Engineering, 30, pp, 471-485, 2003.

[15] G.Campa, J.Wilkie and M.Innocenti, "Robust control and analysis of a towed underwater vehicle," Int. J. Adapt. Control Signal Process., 12, pp. 689-716, 1998.

[16] H.Kajiwara, W.Koterayama, S.Yamaguchi, T.Yokobiki, "Robust control system design for a towed underwater vhicle," Proceedings of INTERNATIONAL SYMPOSIUM ON UNDERWATER TECHNOLOGY, pp, 213 - 216, 2002.

[17] N.Kato, "Underwater Towed Vehicle Maneuverable in Both Vertical and Horizontal Axis (Part1:Principal Configuration and Attitude Control)," The Society of Naval Architects of Japan, no. 169, pp. 111-122, 1991, in japanese.

[18] N.Kato, "Guidance and control of underwater towed vehicle maneuverable in both vertical and horizontal axis," Proc. Second Int. Offshore Polar Eng. Conf., pp. 505-512, 1992.

[19] M.Nakamura, H.Kajiwara, W.Koterayama, "Development of an ROV operated both as towed and self-propulsive vehicle," Ocean Engineering, 28, pp, 1-43, 2000.

[20] M.Toda, "A Theoretic Analysis of Control System Structure of Towed underwater vehicles," 2005 44th IEEE Conference on Decision and Control European Control Conference, Vol. 1-8 pp. 7526-7533, 2005.

[21] J.Wu, J.Ye, C.Yang, Y.Chen, H.Tian, X.Xiong, "Experimental study on a controllable underwater towed system," Ocean Engineering, 32, pp, 1803-1817, 2005.

[22] D.Hopkin, M.Davis and I.Gartshore, "The aerodynamics and control of a remotely-piloted underwater towed vehicle," Canadian Aeronautics and Space Journal, vol. 36, no. 3, pp. 122-129, 1990.

[23] J.M.Preston, "Stability of Towfish used as Sonar Platforms," OCEANS, Proceedings of Mastering the Oceans Through Technology, vol. 2, pp, 888 - 893, 1992.

[24] E.M.Schuch, A.C.Linklater, N.W.Lambeth, C.A.Woolsey, "Design and Simulation of a Two Stage Towing System," OCEANS, Proceedings of MTS/IEEE, vol. 2, pp, 1705 -1712, 2005.

[25] J.Wu, A.T.Chwang, "Investigation on a two-part underwater manoeuvrable towed system," Ocean Engineering, 28, pp, 1079-1096, 2001.

[26] J.Wu, A.T.Chwang, "Experimental investigation on a two-part underwater towed system," Ocean Engineering, 28, pp, 735-750, 2001.

[27] F.C.Teixeira, A.P.Aguiar, A.M.Pascoal, "Nonlinear control of an underwater towed vehicle," 7th IFAC Conference on Manoeuvring and Control of Marine Craft, Lisbon, Portugal, 2006.

[28] F.C.Teixeira, A.P.Aguiar, A.Pascoal, "Nonlinear adaptive control of an underwater towed vehicle," Ocean Engineering, 37, pp, 1193-1220, 2010.

[29] H.K.Khalil, *Nonlinear Systems*, third ed, Prentice-Hall, 2002.

[30] T.S.Walton, H.Polachek, "Calculation of Transient Motion of Submerged Cables," Mathematics of computation, 14, pp, 27-46, 1960.

[31] Z.Feng and R.Allen, "Evaluation of the effects of the communication cable on the dynamics of an underwater flight vehicle," Ocean Engineering, 31, pp. 1019-1035, 2004.

[32] J.I.Gobat, M.A.Grosenbaugh, "Time-domain numerical simulation of ocean cable structures," Ocean Engineering, 10, pp, 1373-1400, 2006.

[33] I.C.Matulea, A.Nastase, N.Talmaciu, G.Slamnoiu, A.M.Goncalves-Coelho, "On the equilibrium configulation of mooring and towing cables," Applied Ocean Research, 30, pp, 81-91, 2008.

[34] V.K.Srivastava, YVSS. Sanyasiraju, M.Tamsir, "Dynamic Behavior of Underwater Towed-cable in Linear Profile," Int. J. of Scientific Engineering Research, vol. 2, no. 7, pp, 1-6, 2011.

[35] J.-K.Choi, T.Shiraishi, T.Tanaka, H.Kondo, "Safe operation of an autonomous underwater towed vehicle: Towed force monitoring and control," Automation in Construction, 20, pp, 1012-1019, 2011.

Acknowledgement

I would like to express my deeply gratitude to Prof. M. Toda for his support and suggestions which were essential for my work. I also owe an important debt to Prof. S. Kametani and Prof. H. Sakai for giving me advice and comments to my study.

I am also grateful to our laboratory members for their warm encouragemant and, finally, special thanks to all the staff in Mastr's Course of Marine System Engineering for permitting the chance and taking care to complete this research.